Nano Research

Open Access

Review Article

Addressing the kinetic imbalance in electrocatalytic C–N coupling: Catalyst design for selective urea synthesis

Qian Xiao[1,2], Chang Chen[1], Di Li[1,2], Jiayu Zhao[1,2], Yani Chai[1,2], Jiawei Wan[1,2] ✉, Ranbo Yu[3] ✉, and Dan Wang[1,2,3] ✉

[1] *State Key Laboratory of Biopharmaceutical Preparation and Delivery, Institute of Process Engineering, Chinese Academy of Sciences, Beijing 100190, China*
[2] *University of Chinese Academy of Sciences, Yuquan Road, Beijing 100049, China*
[3] *College of Chemistry and Environment Engineering, Shenzhen University, Shenzhen 518060, China*

Cite this article: *Nano Research*, **2026**, *19*, 94908662. https://doi.org/10.26599/NR.2026.94908662

ABSTRACT: Electrocatalytic synthesis of urea from CO_2 and NO_3^- provides a promising sustainable decarbonization pathway for fertilizer production. However, its efficiency is hindered by the sluggish C–N coupling kinetics and the intrinsic kinetic imbalance between gaseous CO_2 and aqueous NO_3^-. To address these challenges, this review systematically summarizes recent advances in mechanistic studies and catalytic strategies aimed at resolving the kinetic imbalance in C–N coupling. We start by introducing fundamental parameters and potential mechanisms of electrocatalytic urea production by C–N coupling. Subsequently, we focus on catalyst design, detailing core strategies including dual-site synergy, tandem catalysis, dynamic active site engineering and spatial confinement effects, which collectively work to modulate reaction kinetics and promote the selective coupling of intermediates. Additionally, the design of electrolytes and reactors is crucial for optimizing the reaction environment. Although there is still a gap between current performance and industrial requirements, electrocatalytic urea synthesis holds enormous potential as a key pathway for achieving green fertilizer production and carbon neutrality. This potential can be realized through insights into control of scale and spatial structure, operational mechanisms, engineering of the reaction microenvironment, and the establishment of standardized evaluation protocols. Interdisciplinary collaboration and full-chain technological innovation are crucial for advancing this field toward practical applications.

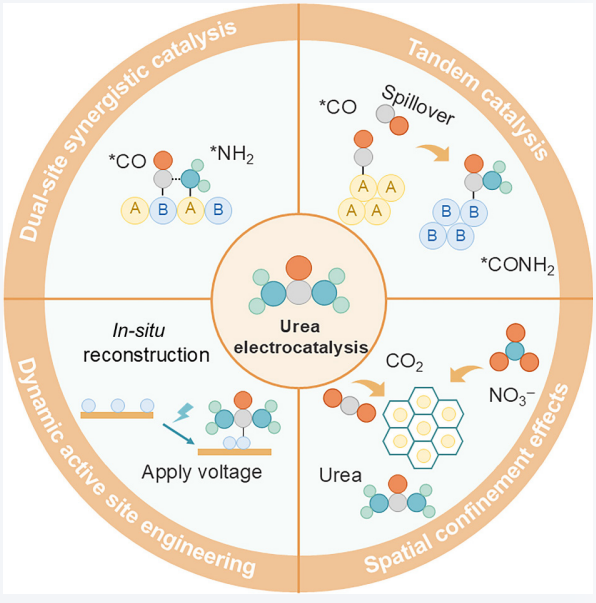

KEYWORDS: electrocatalytic urea synthesis, C–N coupling, addressing the kinetic imbalance, electrocatalyst

1 Introduction

Urea ($CO(NH_2)_2$), is a key industrial precursor and essential nitrogen fertilizer, which plays a crucial role in the chemical sector and global food security. Typically, the production process follows a two-step, high-energy consumption procedure: first, the Haber–Bosch ammonia synthesis process ($N_2 + H_2 \rightarrow NH_3$), and then the Bosch–Meisel process, in which ammonia reacts with carbon dioxide to produce urea ($NH_3 + CO_2 \rightarrow$ Urea) [1–3]. These processes operate under harsh conditions and together account for over 2% of global energy consumption. Urea synthesis consumes about 80% of the ammonia produced worldwide [4–6]. There is an urgent need for sustainable and decentralized alternatives to replace this century-old Bosch–Haber route [7].

The electrocatalytic C–N bond formation driven by renewable electricity provides a highly promising approach to addressing these challenges. By directly electro-catalytically synthesizing urea, using nitrogen-containing substances (such as N_2, NO, NO_2^-, NO_3^-, NH_3, etc.) and carbon-containing substances (such as CO_2, CO,

Received: February 26, 2026; **Revised:** March 16, 2026
Accepted: March 22, 2026

✉Address correspondence to Jiawei Wan, jwwan@ipe.ac.cn; Ranbo Yu, ranboyu@szu.edu.cn; Dan Wang, danwang@szu.edu.cn

HCOOH, $HCONH_2$, etc.) as green substitutes, which has attracted widespread attention and is regarded as a green alternative solution [8, 9] activation process [10–12]. In contrast, nitrate (NO_3^-) is a widely occurring aquatic pollutant that contributes to eutrophication. It has a relatively low N–O bond energy (204 kJ·mol^{-1}), making it a more reactive and attractive nitrogen source for C–N coupling [9, 13]. Equally important is the role of CO_2 as the carbon feedstock. As a major greenhouse gas, its electrochemical conversion can not only provide a sustainable carbon feedstock for value-added chemicals but also mitigate climate impact [14, 15]. This makes NO_3^- an excellent nitrogen source, which allows the electrocatalytic coupling of CO_2 and NO_3^- to serve as the ideal model system for probing the C–N coupling mechanism underlying urea synthesis. By utilizing renewable electricity as the driving force, this process can operate under ambient conditions, compliant with the carbon neutrality goal [16–19].

The electrocatalytic synthesis pathway of urea is competitive thermodynamically and kinetically with a multitude of parallel reduction pathways for CO_2 and NO_3^- separately. This complex reaction network involving multiple parallel pathways is the main reason for the generally low Faradaic efficiency (FE) in urea production. The main reactions leading to urea formation from CO_2 and NO_3^-, as well as the key competitive side reactions, are summarized in the below (V vs. SHE) (pH = 0) [20–22]

$$2NO_3^- + CO_2 + 18H^+ + 16e^- \rightarrow CO(NH_2)_2 + 7H_2O \quad E^0 = 0.85\ V$$

$$2H^+ + 2e^- \rightarrow H_2 \qquad E^0 = 0.00\ V$$

$$CO_2 + 2H^+ + 2e^- \rightarrow HCOOH \qquad E^0 = -0.07\ V$$

$$CO_2 + 2H^+ + 2e^- \rightarrow CO + H_2O \qquad E^0 = -0.06\ V$$

$$2CO_2 + 12H^+ + 12e^- \rightarrow C_2H_5OH + 3H_2O \qquad E^0 = 0.10\ V$$

$$2NO_3^- + 9H^+ + 8e^- \rightarrow NH_3 + 3H_2O \qquad E^0 = -0.12\ V$$

The electrocatalytic synthesis of urea from CO_2 and NO_3^-, despite a deceptively thermodynamic potential ($E^0 \approx 0.85$ V vs. SHE), is severely hampered by its profound kinetic complexity. This process involves a more intricate reaction network than its constituent half-reactions, with its core challenges stemming from:

(1) Sluggish kinetics of C–N coupling: The formation of urea involves multiple electron–proton transfer steps and is a complex multi-step process [23–25]. The parallel reduction of CO_2 and NO_3^- generates a diverse array of reactive intermediates (e.g., *CO, *COOH from CO_2; *NH_2, *NO from NO_3^-), which must encounter and couple at the catalyst surface within their limited lifetimes [26]. The main challenge in achieving high selectivity is the complex competition between C–N coupling and independent hydrogenation pathways, which is largely influenced by the catalyst's ability to co-stabilize key reaction intermediates. When the catalyst exhibits an imbalance in the adsorption strength for CO_2-derived intermediates (*CO, COOH) and NO_3^--derived intermediates (NH_2, *NO), the reactants tend to preferentially proceed through separate reduction pathways, generating a large amount of by-products (such as CO, HCOOH, NH_3) and resulting in a low Faradaic efficiency for urea [27, 28].

(2) Mismatch of reactant concentrations: The co-reduction system involves a gas–liquid–solid three-phase interface, where inherent mass transfer limitations lead to kinetic imbalance. Because the diffusion rate of gaseous CO_2 to the catalyst surface is inherently slower than that of aqueous NO_3^- ions [29, 30]. The local concentration of NO_3^- is higher and it is consumed more rapidly, thereby accelerating the nitrate reduction reaction (NO_3RR) rather than the CO_2 reduction reaction (CO_2RR). Consequently, this imbalance promotes the formation of downstream products of NO_3RR (such as NH_3, NO_2^-, and N_2), undermining the targeted C–N coupling. Although gas diffusion electrodes (GDEs) in flow cells can partially alleviate the mass transport limitations of carbon dioxide, challenges such as water flooding and carbonate formation still persist. The fundamental issue of mismatched reactant supply and local concentration remains a key barrier to achieving high Faradaic efficiency and yield in urea production.

Innovative catalyst design and system engineering are crucial for overcoming these challenges. The central focus is on addressing the intrinsic kinetic imbalance between CO_2 reduction and NO_3^- reduction, which severely limits the efficiency of C–N coupling. This review aims to provide an important overview of the latest advances and strategic insights in the field of electrocatalytic urea synthesis from CO_2 and NO_3^-, with particular emphasis on catalyst design that coordinates the differing reaction kinetics of the two feedstocks (Fig. 1). This review will first introduce the fundamental evaluation parameters and elucidate the basic reaction mechanisms. Subsequently, it will systematically analyze emerging catalyst design strategies, including dual-site synergistic catalysis, tandem catalysis, dynamic active site engineering, and spatial confinement effects, which are crucial for promoting the synchronous activation of C and N intermediates and their selective coupling. Thereafter, this review will explore the crucial role of electrolyte engineering and advanced reactor design in optimizing the local reaction microenvironment, aiming to further mitigate kinetic and mass transfer mismatches, thereby improving yield, selectivity, and future industrial applicability. Concluding with an outlook, this review will highlight the key technical hurdles and emerging opportunities that will shape the future of this field, from fundamental mechanistic understanding to scalable process integration.

2 Fundamental parameters and potential mechanisms of electrocatalytic urea production by C–N coupling

2.1 Fundamental parameters of electrocatalytic urea production by C–N coupling

2.1.1 *Faradaic efficiency*

In electrocatalytic urea production, FE refers to the proportion of electrons used for producing urea ($CO(NH_2)_2$) relative to the total electron consumption, which is the electron efficiency for the product selectivity [13]. FE largely reflects the electron utilization efficiency and can be calculated by Eq. (1)

$$FE\ (\%) = \frac{Q_{urea}}{Q_{total}} \times 100\% = \frac{n \times F \times c \times V}{M \times Q_{total}} \times 100\% \qquad (1)$$

where Q_{urea} (C) is the charge consumed for urea production during the electrocatalytic process. The calculation of Q_{urea} is generally: Electron Transfer Number × Total Urea Production Concentration.

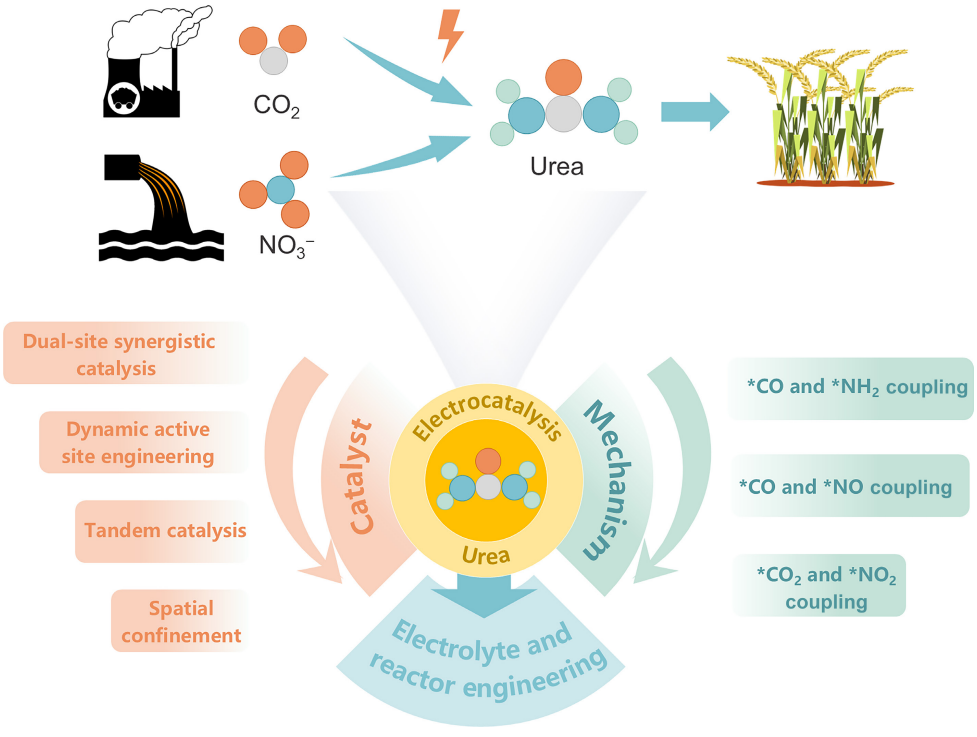

Figure 1 Schematic overview of electrocatalytic urea synthesis from CO_2 and NO_3^-, highlighting the key challenges (sluggish C–N coupling kinetics and reactant concentration mismatch) and the corresponding catalyst design strategies (dual-site synergy, tandem catalysis, dynamic active site engineering, and spatial confinement) that promote selective C–N bond formation. The major C–N coupling pathways and competing side reactions are depicted, along with the complementary roles of electrolyte and reactor engineering in optimizing the reaction microenvironment.

For the detection of urea production concentration, current methods include the urease method, the diacetyl monoxime (DAMO) method, and nuclear magnetic resonance (NMR). Q_{total} (C) represents the total charge passed during electrolysis, obtained by integrating the chronoamperometric current over time, n is the electron transfer number. When CO_2 and NO_3^- are used as raw materials, there is generally a 16-electron transfer, F is the Faraday constant (96,485 C·mol^{-1}), c (mol·L^{-1}) is the concentration of urea, V (L) is the volume of electrolyte, and M (g mol^{-1}) is the molecular mass of urea.

2.1.2 Overpotential

Overpotential refers to the extra potential beyond the thermodynamic equilibrium potential required to drive an electrochemical reaction, reflecting the kinetic energy barrier of the process. A lower overpotential corresponds to faster reaction kinetics [31]. For the electrocatalytic synthesis of urea from CO_2 and NO_3^-, the theoretical thermodynamic potential is approximately 0.85 V vs. SHE. Operating closer to this theoretical potential minimizes overpotential and thus improves energy conversion efficiency. However, in practice, the complex multi-step kinetics and numerous competing side reactions often lead to significant overpotentials, resulting in relatively low FE and urea yield under realistic electrolysis conditions [13].

2.1.3 Urea yield rate

The urea yield rate is a crucial parameter, which can directly reflect the reaction rate of electrocatalytic urea production. Typically, a normalization method is employed to account for catalyst mass or electrode surface area in order to compare the catalytic performance of different catalysts. The urea yield rate can be calculated by Eq. (2)

$$R_{urea} = \frac{CV}{tS} \quad (2)$$

where C is the urea concentration, V is the volume of electrolyte, t is the electrolysis time, and S is the geometric area of the working electrode or catalyst loading mass. To meet the requirements of industrial scale-up, a urea yield of > 1 mol·h^{-1}·g^{-1} or higher is generally needed [32]. Currently, the urea yield rate in most studies remains at the level of μmol·h^{-1} to mmol·h^{-1}·g^{-1}, and it is necessary to improve the yield by at least 3–4 orders of magnitude to have industrialization potential [8].

2.1.4 Selectivity

Selectivity refers to the amount of urea produced relative to other by-products during the urea synthesis process. For the electrocatalytic synthesis of urea from CO_2 and NO_3^-, the by-products of the CO_2 reduction pathway include CO, HCOOH, CH_4, C_2H_4 etc., while the by-products of the NO_3^- reduction pathway include NH_3, N_2, NO_2^-, etc. In addition, the hydrogen evolution reaction (HER) generates a large amount of H_2, which reduces the carbon and nitrogen utilization efficiency [33]. The selectivity in urea synthesis is often categorized as N_{urea}-selectivity and C_{urea}-selectivity, which reflect the conversion efficiencies of CO_2 and NO_3^- into urea, respectively. The N_{urea}-selectivity represents the molar proportion of urea to all N-containing products and the C_{urea}-selectivity refers to the molar proportion of urea to all C-containing products, which can be calculated by Eqs. (3) and (4) [34]

$$N_{urea}\text{-selectivity} = \frac{n_{urea}(N)}{n_{total}(N)} \quad (3)$$

$$C_{urea}\text{-selectivity} = \frac{n_{urea}(C)}{n_{total}(C)} \quad (4)$$

2.1.5 *Stability*

Stability refers to the ability of a catalyst to maintain its activity and structural stability during long-term operation or multiple cycles, which is a key indicator for industrial applications. The stability of an electrocatalyst is reflected by its ability to maintain a consistent current density over extended reaction time, which is typically assessed through long-term potentiostatic or galvanostatic tests. The urea cycling performance test can be conducted through long-term electrocatalytic experiments under a constant potential (typically exceeding 100 h) or 12 repeated cycles (0.5 or 1 h per cycle). The stability of the catalyst is evaluated by monitoring whether the urea yield, FE, and current density decrease over time. Industrial catalysts are required to maintain catalytic activity over thousands of hours. In contrast, laboratory-scale assessments usually cover only a duration of a few hours to tens of hours, indicating that current testing protocols have not yet satisfied the rigorous standards required for industrial-scale.

2.2 Mechanisms of electrocatalytic urea production by C–N coupling

A fundamental understanding of the C–N coupling mechanism can guide the rational design of high-performance catalysts and is crucial for the electrocatalytic synthesis of urea from CO_2 and NO_3^-. Currently, mechanistic studies are primarily conducted through the synergistic use of advanced *in-situ* techniques, such as infrared and Raman spectroscopy, and density functional theory (DFT) calculations. Researchers can use these methods to detect key intermediates and simulate reaction pathways in real time. To date, three major C–N coupling pathways have been widely proposed and studied: (i) coupling between *CO and *NH_2, (ii) coupling between *CO and *NO, and (iii) coupling between *CO_2 and *NO_2. The following section establishes a clear structure–activity relationship through a detailed introduction of mainstream mechanisms and key experimental observations (Fig. 2) [35–38], and provides actionable guidance for future catalyst engineering.

2.2.1 **CO and *NH_2 Coupling*

The *CO + *NH_2 coupling pathway represents one of the earliest and most extensively studied mechanisms for electrochemical urea formation (Fig. 2(a)). In this route, CO_2 is first reduced to adsorbed *CO, while NO_3^- undergoes sequential hydrogenation to form *NH_2 intermediates on the catalyst surface. The key C–N bond is then established via the coupling of these two adsorbed species, yielding *$CONH_2$ as the primary coupling intermediate, which subsequently undergoes further proton–electron transfers to form urea.

In the early 1990s, Shibata et al. [39, 40] achieved the electrochemical synthesis of urea under ambient conditions via co-reduction of CO_2 and NO_2^-/NO_3^-. Control experiments involving substitution of C and N sources confirmed that free CO and NH_3 in solution cannot form C–N bonds. They proposed that the C–N bond forms through coupling of *CO and *NH_2 on the catalyst—a mechanism supported by the observed correlation between urea yield and the catalyst's independent CO and NH_3 producing activities. However, experimental and theoretical evidence for the existence and coupling of these intermediates remains scarce. Feng et al. [41] investigated the co-reduction of CO_2 and NO_2^- on Te-doped Pd nanocrystals (Te-Pd NCs). DFT calculations reveal that the energy barrier for *CO and *NH_2 coupling to form *$CONH_2$ on the Te-Pd(111) surface (0.92 eV) is significantly lower than that on pure Pd(111) (1.46 eV), confirming thermodynamically and kinetically that *CO and *NH_2 serve as key intermediates in C–N bond formation. However, control experiments show that urea is not produced when using ammonia solution as the N source or CO gas as the C source, which appears inconsistent with the proposed *CO and *NH_2 intermediate mechanism. Wang et al. [42] investigated the reaction mechanism of electrocatalytic urea synthesis through the co-reduction of CO_2 and NO_3^- on a Cu/ZnO tandem gas-diffusion electrode. Using *in situ* Raman spectroscopy, the authors detected δ(CN) and ν(CN) vibration peaks at 562 and 1024 cm^{-1}, respectively (Fig. 3(a)), indicating the formation of C–N bonds. Meanwhile, attenuated total reflection Fourier transform infrared spectroscopy (ATR-FTIR) spectroscopy revealed an asymmetric vibration peak of the C–N bond in urea at 1469 cm^{-1} (Fig. 3(b)), further confirming urea generation. Additionally, nitrogen-containing intermediates such as *NO_2 and *NH_2 were observed, with their signal intensities significantly enhanced on the $Cu_{1.0}/ZnO_{0.5}$ electrode. CO_2 is selectively reduced to CO on the ZnO segment, while nitrate undergoes multistep hydrogenation on the Cu segment to form *NH_2. Subsequently, C–N coupling between *CO and *NH_2 produces the *$CONH_2$ intermediate, which ultimately undergoes a second C–N coupling step to form urea. However, no *CO signal was detected during *in-situ* measurements, and insufficient control experiments with different feedstocks were conducted, indicating that further work is needed to fully understand the C–N coupling mechanism. Sun et al. [43] developed a plasma-electrocatalytic coupling route, which starts with plasma-assisted air activation to generate reactive NO_x^-, followed by electrocatalytic co-reduction of CO_2 and NO_x^- to urea.

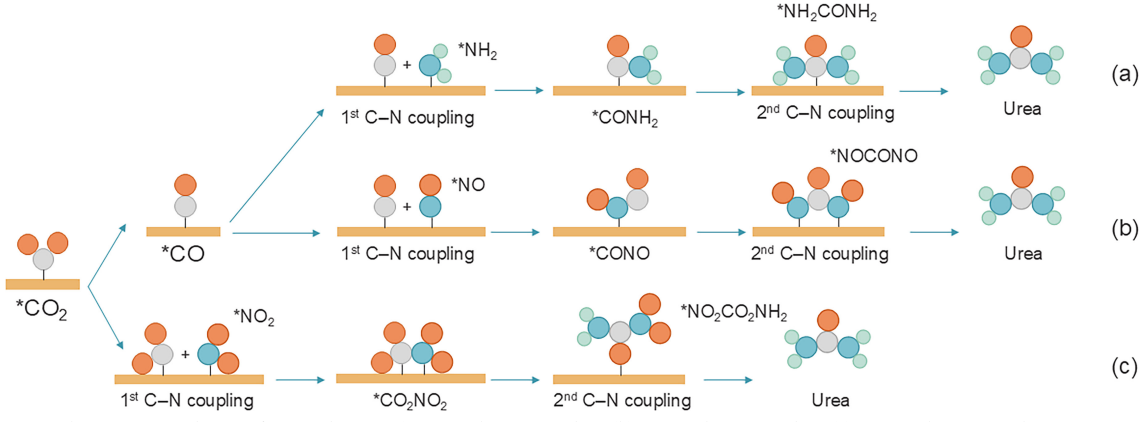

Figure 2 C–N coupling reaction pathways of CO_2 with NO_3^- (a) *CO and *NH_2 coupling. (b) *CO and *NO coupling. (c) *CO_2 and *NO_2 coupling.

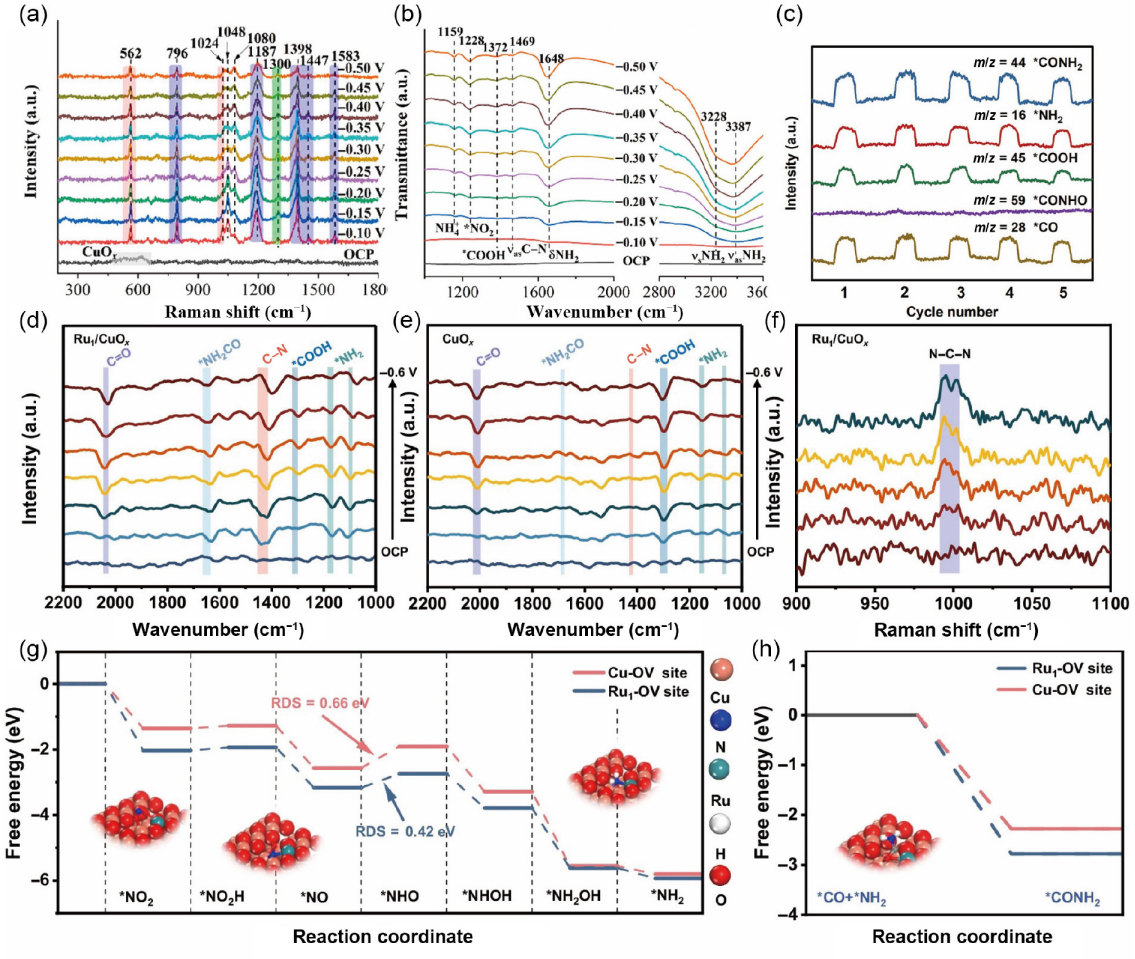

Figure 3 (a) *In-situ* Raman spectra of Cu/ZnO. (b) *In-situ* ATR-FTIR spectra of Cu/ZnO. Reproduced with permission from Ref. [42], © American Chemical Society 2023. (c) Online DEMS spectra of Ru_1/CuO_x at −0.6 V. (d) and (e) *In-situ* FTIR spectra of Ru_1/CuO_x and CuO_x. (f) *In-situ* Raman spectra of Ru_1/CuO_x. (g) NO_2 → $*NH_2$ pathways. (h) Schematic illustration of *CO and $*NH_2$ coupling for C–N bond formation on Cu-OV and Ru_1-OV sites. Reproduced with permission from Ref. [43], © Sun, Z. Y. et al. 2025.

Online differential electrochemical mass spectrometry (DEMS) detection identified key intermediates such as $*CONH_2$, $*NH_2$, and *CO, excluding the *CONHO pathway and directly supporting *CO and $*NH_2$ as the C–N coupling precursors (Fig. 3(c)). *In-situ* FTIR detected signals at 1415 cm^{-1} (C–N coupling bond) and 1634 cm^{-1} ($CONH_2$), confirming the formation of C–N bonds. Meanwhile, Raman spectroscopy showed a significantly enhanced N–C–N bond signal, collectively evidencing the C–N coupling process (Figs. 3(d)–3(f)). Theoretical calculations indicated that Cu-OV sites preferentially activate CO_2 to *CO, while Ru_1-OV sites activate NO_2^- to $*NH_2$, and the migration of *CO from Cu-OV sites to Ru_1-OV sites for coupling with $*NH_2$ is energetically more favorable (Figs. 3(g) and 3(h)).

The *CO-$*NH_2$ coupling pathway is theoretically favorable on modified catalysts and supported by direct evidence from advanced techniques like DEMS [44]. However, experimental verification is often incomplete due to the lack of direct *in-situ* detection of these intermediates and inconsistencies in control experiments. Future efforts require more sensitive *operando* spectroscopy and precisely designed validation to dynamically trace this coupling process.

2.2.2 *CO and *NO coupling

The *CONO coupling mechanism theoretically offers potential advantages such as a shorter pathway, higher energy efficiency, and superior selectivity. Nevertheless, its detailed mechanistic steps require further clarification and extensive investigation. The reaction pathway proceeds through the key intermediates: *ONCO → *ONCONOH → $*NHCONH_2$ → urea (Fig. 2(b)).

Experimental evidence for this C–N coupling pathway is supported by several catalyst systems. Wei et al. [45] developed the oxygen vacancy-enriched CeO_2 electrocatalyst that stabilizes the *NO intermediate at Vo sites and promotes its direct coupling with *CO to form *OCNO, ultimately leading to product urea. *In-situ* sum frequency generation (SFG) spectroscopy detected the characteristic signals of generated *NO (1888 cm^{-1}) and the key coupling intermediate *OCNO (2120 cm^{-1}) (Fig. 4(a)), providing direct experimental evidence for the proposed mechanism. DFT calculations further revealed that the energy barrier for coupling *NO with *CO to form *OCNO on Vo sites is only 0.27 eV, which is much lower than that of the competing protonation pathway, confirming the kinetic advantage of this route (Fig. 4(b)). Together, this evidence supports a novel reaction pathway in which Vo stabilizes *NO and facilitates its early coupling with *CO (the *CONO pathway). Tu et al. (Figs. 4(c)–4(e)) [46] demonstrated that alkali metal cations (especially K^+) at the electrode/electrolyte interface assemble intermediates, activating C–N coupling.

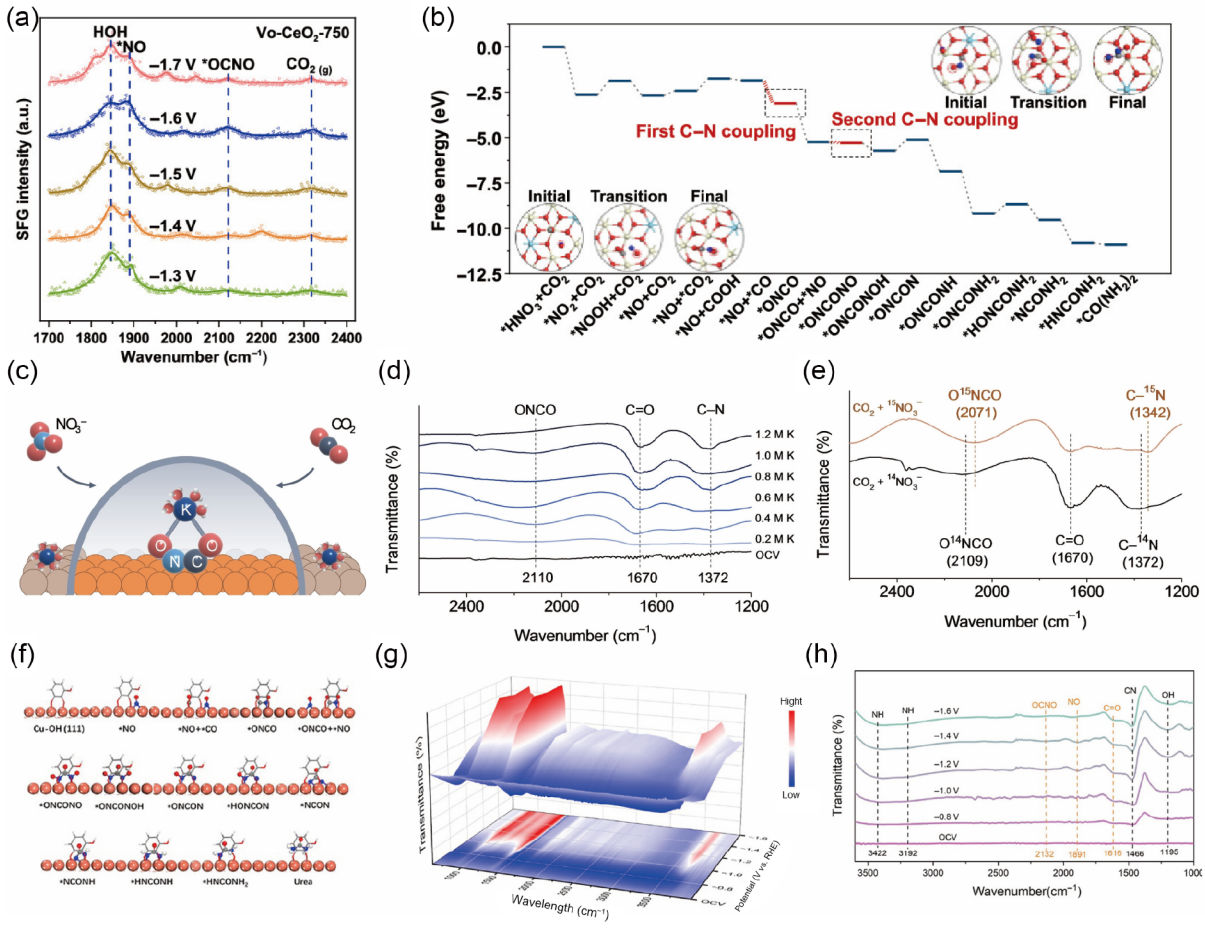

Figure 4 (a) SFG signals of intermediate species on Vo-CeO_2-750. (b) Corresponding free-energy profile for urea formation on Vo-enriched CeO_2. Reproduced with permission from Ref. [45], © American Chemical Society 2022. (c) Schematic illustrating the role of K^+ in promoting C–N coupling and the generation of the *ONCO intermediate. (d) Infrared spectra in the range of 1200–2600 cm^{-1} at −1.5 V vs. RHE during co-electrolysis in electrolytes containing various concentrations of K^+. (e) Isotope-labelling infrared signal in the range of 1200–2600 cm^{-1} at −1.5 V vs. RHE. Reproduced with permission from Ref. [46], © Wiley-VCH GmbH 2023. (f) The optimized geometric structures of the intermediates involved in urea synthesis on the Cu-OH(111) surface. (g) 3D FTIR spectra for electrocatalytic C–N coupling over Cu-OH. (h) Infrared signal in the range of 1000–3600 cm^{-1} under the negatively shifted potentials from −0.8 to −1.6 V vs. RHE for Cu-OH. Reproduced with permission from Ref. [47], © Wiley-VCH GmbH 2025.

Operando synchrotron-radiation Fourier transform infrared spectroscopy (SR-FTIR) identified the key intermediate *ONCO (~ 2110 cm^{-1}), with isotopic experiments (using $^{15}NO_3^-$) inducing a ~ 30 cm^{-1} redshift, robustly verifying its authenticity. Chen et al. [47] engineered a $Cu^{\delta+}/Cu^0$ interface via molecular modification with tannic acid (Figs. 4(f)–4(h)). *Operando* SR-FTIR detected signatures of *OCNO (2132 cm^{-1}), *NO (1891 cm^{-1}), and the C–N bond (1466 cm^{-1}), providing direct spectroscopic evidence for the coupling process.

These studies collectively highlight that, unlike the conventional CO-NH_2 coupling, the *CONO pathway is a reliable and efficient route for electrocatalytic urea synthesis. The convergence of advanced *in-situ* spectroscopy and theoretical modeling across diverse catalytic systems strongly validates the mechanism of early C–N coupling via nitrogenous intermediates.

2.2.3 *CO_2 and *NO_2 coupling

The possible C–N coupling pathway is that *CO_2 adsorbed on the catalyst surface directly participates in C–N coupling without being converted to *CO [48]. The reaction pathway proceeds through the key intermediates: *CO_2NO_2 → *$CONH_2$ → *NO_2CONH_2 → urea (Fig. 2(c)).

Lu et al. [25] demonstrated selective electrocatalytic urea synthesis from NO_3^- and CO_2 using $In(OH)_3$ catalysts with exposed facets. *In-situ* SR-FTIR revealed a C–N stretching vibration at 1419 cm^{-1} along with –NH_2 bending (1635 cm^{-1}) and wagging (1170 cm^{-1}) modes, confirming C–N bond formation and urea-related intermediates. DFT calculations indicated that the facets promote direct C–N coupling between *NO_2 and *CO_2 at an early stage, exhibiting a lower energy barrier (0.35 eV) compared to the *NO_2 protonation pathway (0.62 eV), thereby favoring urea production over NH_3 by-products. Chen et al. [49] verifies the C–N coupling mechanism of *CO_2NO_2 by combining DFT calculations and *operando* FTIR spectroscopy (Figs. 5(a) and 5(b)). DFT results show that the Pd_1-Cu site facilitates the early C–N coupling between *NO_2 and *CO_2 to form *CO_2NO_2 with the lowest energy barrier, while *operando* FTIR detects key intermediates such as *CO_2NH_2 and *$COOHNH_2$, confirming the tandem catalytic pathway on $CuPd_1Rh_1$-DAA. Wang et al. [50] elucidated the reaction mechanism of CO_2 as the direct C source in electrocatalytic urea synthesis through combined experimental and theoretical investigations. On Cu/Zn oxide tandem gas-diffusion electrodes, control experiments demonstrated that only CO_2 enables highly selective urea formation, ruling out CO or HCOOH as key

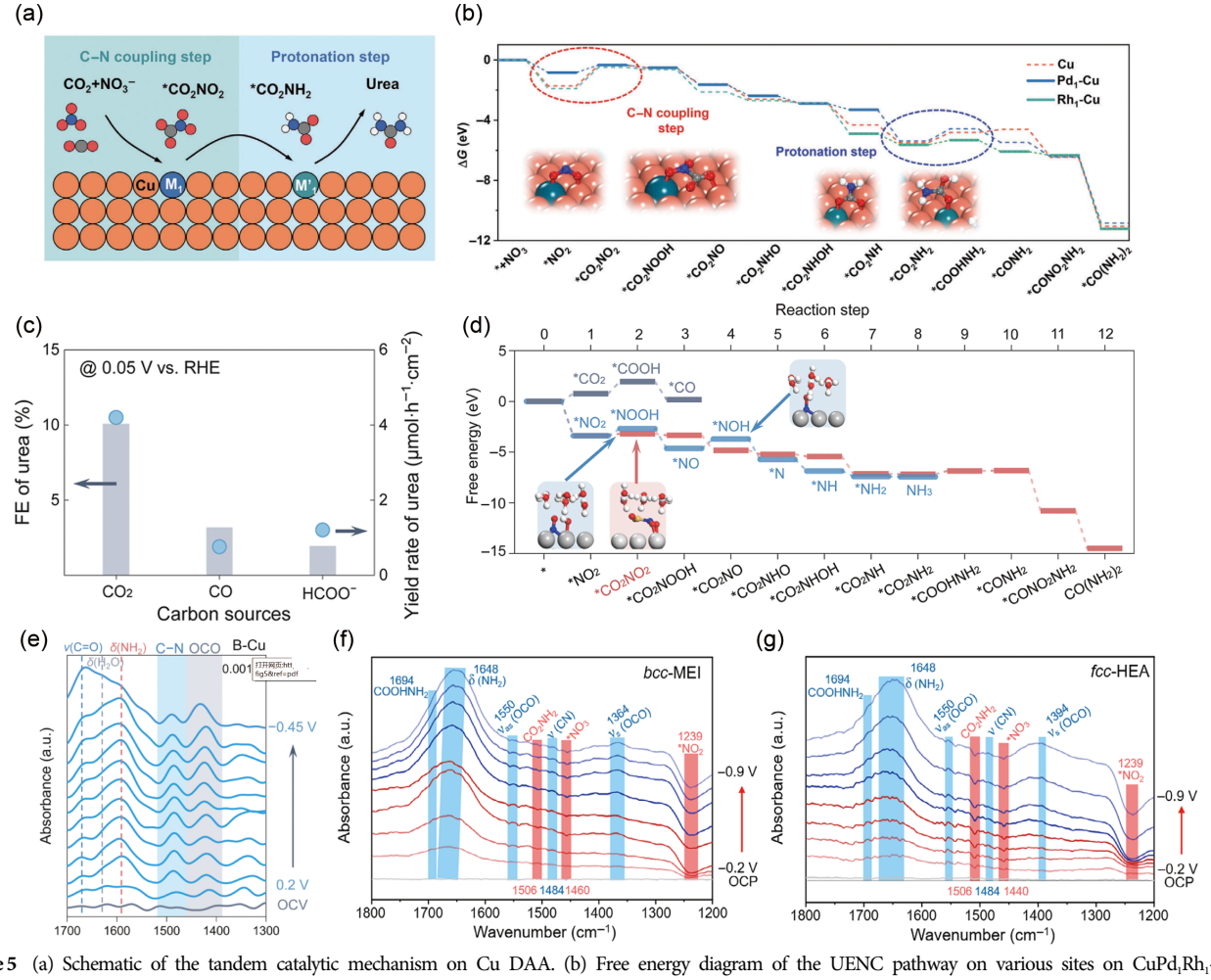

Figure 5 (a) Schematic of the tandem catalytic mechanism on Cu DAA. (b) Free energy diagram of the UENC pathway on various sites on $CuPd_1Rh_1$-DAA. Reproduced with permission from Ref. [49], © Wiley-VCH GmbH 2024. (c) Urea FE and yield rate on Cu using different carbon sources at 0.05 V vs. RHE. (d) DFT-derived free-energy profiles for individual CO_2 reduction, nitrate reduction and their coupled pathway toward urea formation. (e) *In situ* ATR-FTIR measurements on B-Cu. Reproduced with permission from Ref. [50], © American Chemical Society 2025. *Operando* ATR-SEIRAS spectra of (f) fcc-HEA and (g) bcc-MEI under various potentials. Reproduced with permission from Ref. [51], © Wiley-VCH GmbH 2025.

intermediates (Fig. 5(c)). DFT calculations revealed that the coupling of $*NO_2$ with CO_2 is thermodynamically more favorable than $*NO_2$ hydrogenation to ammonia, and reducing the adsorption energy of $*NO_2$ promotes Eley–Rideal type coupling with weakly adsorbed or free CO_2 molecules (Fig. 5(d)). *In-situ* ATR-FTIR spectroscopy and $^{15}NO_3^-$ isotopic labeling experiments directly confirmed that the C–N bond in urea originates from the direct coupling between CO_2 and nitrate reduction intermediates (Fig. 5(e)). This mechanistic understanding guided the design of boron-doped Cu catalysts, in which tuning the electronic structure of Cu enhances the selective coupling between CO_2 and $*NO_2$. Chen et al. [51] revealed the critical role of the $*CO_2NO_2$ intermediate and its regulation mechanism in the electrochemical synthesis of urea. *In-situ* attenuated total reflection aurface-enhanced infrared absorption spectroscopy (ATR-SEIRAS) and Raman spectroscopy directly captured signals of C–N coupling intermediates ($*CO_2NH_2$, $*COOHNH_2$) and urea formation (Figs. 5(f) and 5(g)). Performance comparisons demonstrated that the HEA primarily produced urea and NO_2^-, whereas the ordered medium-entropy intermetallic MEI tended to deeply hydrogenate $*NO_2$ to NH_3, highlighting structural control over the reaction pathway.

Recent studies consistently validate the $*CO_2NO_2$-mediated pathway for urea synthesis. While *in-situ* spectroscopy and DFT calculations have identified downstream C–N species and lower energetic barriers, direct detection of transient intermediates ($*CO_2$, $*NO_2$, $*CO_2NO_2$) remains a key experimental gap. Advancing this understanding requires *operando* techniques with higher temporal and spatial resolution, coupled with dynamic theoretical simulations, to fully elucidate the real-time reaction pathway.

Although $*CONH_2$, *CONO, and $*CO_2NO_2$ represent the most widely studied C–N coupling pathways in electrocatalytic urea synthesis, other plausible routes (e.g., involving *CONOOH or $*CONO_2$) have also been proposed, underscoring the complexity and diversity of the reaction network. Direct experimental confirmation of these transient intermediates and real-time tracking of C–N bond formation remains challenging, however, due to their short lifetimes, low concentrations, and interference from parallel side reactions. To unambiguously establish the operative mechanisms and uncover possible hidden pathways, future work should focus on advancing and integrating *operando* techniques with higher spatiotemporal resolution—such as time-resolved IR/Raman spectroscopy, synchrotron-based X-ray spectroscopy, and online mass spectrometry—together with multiscale

simulations and machine-learning-aided dynamic modeling. This combined approach is crucial for achieving a comprehensive understanding of C–N coupling and for guiding the rational design of next-generation catalysts with improved urea electrosynthesis activity and selectivity.

3 The design strategies of catalysts

Due to the intense competition from the independent reduction pathways of CO_2 and NO_3^-, electrocatalytic urea synthesis via C–N coupling faces challenges of slow kinetics and low selectivity. The inherent kinetic differences between CO_2RR and NO_3RR present a major obstacle, resulting in asynchronous reaction rates, varying adsorption energies of key intermediates, and heterogeneous local reactant concentrations. This imbalance severely hinders the synchronized activation of carbon and nitrogen intermediates and their selective coupling, leading to the preferential formation of by-products (such as CO and NH_3) rather than the desired C–N bonds. In order to coordinate these disparate kinetics and steer the reaction network to efficiently form urea, customized catalyst design is imperative. This review first consolidates the reported performance metrics for the conversion of CO_2/NO_3^--to-urea (Table 1). Based on these data, we emphasize that effective catalyst design must proactively address the kinetic mismatch between CO_2RR and NO_3RR by promoting the simultaneous activation and selective coupling of C- and N-intermediates. By summarizing the investigations and property classifications of these published catalysts, they can be divided into these different strategies, including dual-site synergistic catalysis, tandem catalysis, dynamic active site engineering, spatial confinement effects, the synergistic role of catalyst supports, and other emerging approaches (Fig. 6). Each strategy offers distinct pathways to modulate the reaction microenvironment and intermediate trafficking to enhance urea selectivity and yield.

3.1 Dual-site synergistic catalysis

Dual-site synergistic design can directly counter the kinetic imbalance between CO_2RR and NO_3RR, where two adjacent active sites are engineered to independently stabilize the key intermediates of each pathway: one site for CO_2 activation and the other for NO_3^-

Table 1 A summary of electrocatalysts for urea synthesis from CO_2 and NO_3^-

Electrocatalyst	N source	Electrolyte	Yield rate	FE (%)	*E* (V vs. RHE)	Reactor	Refs.
Cu/Zn	NO_3^-	0.1 M $KHCO_3$ 500 ppm NO_3^-	16 μmol·h^{-1}·cm^{-2}	75%	−0.6	Flow-cell	[52]
$In(OH)_3$-S	NO_3^-	0.1 M KNO_3	8.89 mmol·g^{-1}·h^{-1}	53.4%	−0.6	H-cell	[25]
Cu/PI (PI polyimide)	NO_3^-	0.1 M KNO_3 0.1 M $KHCO_3$	255.0 mmol·g^{-1}·h^{-1}	12%	−1.4	H-cell	[53]
$NiCeO_{2-x}$	NO_3^-	CO_2-saturated 0.1 M KNO_3	36.25 mmol·g^{-1}·h^{-1}	70.10%	−0.5	H-cell	[54]
PCOF-34-Fe	NO_3^-	0.1 M KNO_3 0.1 M $KHCO_3$	17 mmol·g^{-1}·h^{-1}	90.00%	−0.5	H-cell	[55]
	NO_3^-	0.1 M KNO_3 0.1 M $KHCO_3$	135.6 mmol·g^{-1}·h^{-1}	51.30%	−0.6	Flow cell	
Pd_2Au_1/RuO	NO_3^-	0.05 M KNO_3 0.2 M $KHCO_3$	73.5 mmol·g^{-1}·h^{-1}	75.60%	−0.5	Flow cell	[56]
Fe-TPP/CNT hybrids	NO_3^-	0.1 M KNO_3 0.2 M $KHCO_3$	6.57 mmol·g^{-1}·h^{-1}	27.7%	−0.2–−0.8	H-cell	[57]
Ti-DHTP	NO_3^-	0.1 M KNO_3 0.5 M K_2SO_4	348.0 μg·h^{-1}·cm^{-2}	21.7%	−0.6	H-cell	[58]
$CuPd_1Rh_1$ diatomic alloys	NO_3^-	0.1 M KNO_3 0.1 M $KHCO_3$	53.2 mmol·g^{-1}·h^{-1}	72.10%	−0.5	Flow cell	[49]
Au@cpCu$_7$CF	NO_3^-	0.008 M KNO_3 0.2 M K_2SO_4	2.10 mmol·g^{-1}·h^{-1}	55.53%	−0.2–−0.6	H-cell	[59]
TiO_2-C	NO_3^-	0.1 M KNO_3	43.4 mmol·g^{-1}·h^{-1}	48.80%	−0.9	Flow cell	[60]
$CuWO_4$	NO_3^-	0.1 M KNO_3	1.6 mmol·g^{-1}·h^{-1}	70.10%	−0.2	H-cell	[27]
Cu-CeO_2	NO_3^-	0.05 M KNO_3 0.1 M $KHCO_3$	52.84 mmol·g^{-1}·h^{-1}	5%	−1.6	H-cell	[61]
Cu-MnO_2	NO_3^-	0.05 M KNO_3 0.1 M $KHCO_3$	78 mmol·g^{-1}·h^{-1}	54.7%	−0.5	Flow cell	[62]
Mo-PCN-222(Co)	NO_3^-	0.05 M KNO_3 0.1 M $KHCO_3$	14.1 mmol·g^{-1}·h^{-1}	33.90%	−0.4	H-cell	[63]
γ-Fe_2O_3@Ni-HITP	NO_3^-	0.04 M KNO_3 0.1 M $KHCO_3$	245 mmol·g^{-1}·h^{-1}	63.40%	−0.8	Flow cell	[64]
	NO_3^-	0.1 M KNO_3 1 M $KHCO_3$	340 mmol·g^{-1}·h^{-1}	67.20%	−0.8	Flow cell	
SnBiNS/rGO	NO_3^-	KNO_3 0.1 M $KHCO_3$	7.7 mmol·g^{-1}·h^{-1}	78.36%	−0.4	Flow cell	[65]
Diatomic Fe–Ni catalyst	NO_3^-	0.05 M KNO_3 0.1 M $KHCO_3$	20.2 mmol·g^{-1}·h^{-1}	17.8%	−1.5	H-cell	[66]

(Continued)

Electrocatalyst	N source	Electrolyte	Yield rate	FE (%)	*E* (V vs. RHE)	Reactor	Refs.
m-Cu_2O	NO_3^-	0.01 M KNO_3 0.1 M $KHCO_3$	29.2 mmol·g^{-1}·h^{-1}	9.43%	−1.3	H-cell	[67]
Cu/Cu_2O-NRH	NO_3^-	0.1 M KNO_3 0.5 M $KHCO_3$	30.4 μmol·h^{-1}·cm^{-2}	35%	−0.3	H-cell	[68]
Fe(a)@C-Fe_3O_4/ CNTs	NO_3^-	0.1 M KNO_3	22.36 mmol·g^{-1}·h^{-1}	16.5%	−0.65	H-cell	[69]
Zn_1/In_2O_{3-x}	NO_3^-	0.1 M KNO_3 0.1 M $KHCO_3$	41.6 mmol·g^{-1}·h^{-1}	55.8%	−0.7	Flow-cell	[70]
Cu/ZnO	NO_3^-	0.1 M KNO_3	3.2 μmol·h^{-1}·cm^{-2}	37.4%	−0.3	Flow-cell	[42]
Cu–OH	NO_3^-	0.9 M $KHCO_3$ 0.1 M KNO_3	386.4 mmol·g^{-1}·h^{-1}	25.2%	−1.2	H-cell	[47]
B–Cu	NO_3^-	1 M KOH 0.1 M KNO_3	101.2 μmol·h^{-1}·cm^{-2}	80.1%	−0.22	Flow-cell	[50]
fcc-HEA	NO_3^-	0.02 M KNO_3	52.43 mmol·g^{-1}·h^{-1}	22.57%	−0.9	H-cell	[51]
RP-AuCu	NO_3^-	0.1 M $KHCO_3$ 0.1 M KNO_3	22.9 mmol·g^{-1}·h^{-1}	88.5%	−0.6 (FE_{max}) −0.5 ($Yield_{max}$)	H-cell	[71]
Cu-N_3 SA_S	NO_3^-	0.1 M $KHCO_3$ 0.1 M KNO_3	19597.65 μg·h^{-1}·mg_{cu}^{-1}	55.4%	−0.9	H-cell	[72]
CuPPc	NO_3^-	0.9 M $KHCO_3$ 0.1 M KNO_3	460.0 mmol·g^{-1}·h^{-1}	26.1%	−1.3	H-cell	[73]
Cu_2O	NO_3^-	0.1 M $KHCO_3$ 50 mM $NaNO_3$	34.6 mmol·g^{-1}·h^{-1}	17.72 %	−1.5	H-cell	[74]
	NO_3^-	0.1 M $KHCO_3$ 50 mM $NaNO_3$	64.2 mmol·g^{-1}·h^{-1}	> 17.2%	−1.5	Flow-cell	
CuPc-Amino	NO_3^-	0.1 M $KHCO_3$ 0.05 M KNO_3	103.1 mmol·g^{-1}·h^{-1}	11.9%	−1.6	H-cell	[75]
Ru-CeO_2	NO_3^-	0.1 M $KHCO_3$ 0.05 M KNO_3	20.2 mmol·g^{-1}·h^{-1}	20.1%	−0.7	H-cell	[76]
Bi:10%In/C NPs	NO_3^-	0.1 M $KHCO_3$ 0.1 M KNO_3	10.1 mmol·g^{-1}·h^{-1}	20.31%	−0.45	H-cell	[77]
a-$Cu_{0.1}CoB_x$ metallene	NO_3^-	0.1M KNO_3	5.2 mmol·g^{-1}·h^{-1}	27.7%	−0.5	H-cell	[78]
B-FeNi-DASC	NO_3^-	0.1 M $KHCO_3$ 50 mM KNO_3	20.2 mmol·g^{-1}·h^{-1}	17.8%	−1.5	H-cell	[66]
Cu–SiO_2–C_{60}	NO_3^-	—	385.9 mmol·g^{-1}·h^{-1}	27.6%	−1.3	H-cell	[79]
Cu–CeO_2-Vo	NO_3^-	0.1 M $KHCO_3$ 0.1 M KNO_3	59.96 mmol·g^{-1}·h^{-1}	7.75%	−1.55	H-cell	[80]
$CoRuN_6$	NO_3^-	0.1 M KNO_3	8.98 mmol·g^{-1}·h^{-1}	25.31%	−0.6	H-cell	[81]
V_o-InOOH	NO_3^-	0.1 M KNO_3	0.164 mmol·g^{-1}·h^{-1}	51.0%	−0.5	H-cell	[82]
Cu-PMOF	NO_3^-	0.15 M $KHCO_3$ 0.05 M KNO_3	25.5 mmol·g^{-1}·h^{-1}	52.7%	−0.50–−0.55	H-cell	[83]
C–Cu–A_4	NO_3^-	0.9 M $KHCO_3$ 0.1 M KNO_3	890 mmol·g^{-1}·h^{-1}	45.4%	−1.2	H-cell	[84]
$CuSiO_x$	NO_3^-	0.1 M $KHCO_3$ 0.1 M KNO_3	26.77 mmol·g^{-1}·h^{-1}	79.01%	−0.2 (FE_{max}) −0.6 ($Yield_{max}$)	Flow-cell	[85]
W/CuO	NO_3^-	0.1 M $KHCO_3$ 0.1 M KNO_3	86.29 mmol·g^{-1}·h^{-1}	73.52 %	−0.7	Flow-cell	[86]
graphene-In_2O_3	NO_3^-	0.1 M $KHCO_3$ 0.1 M KNO_3	5.958 mmol·g^{-1}·h^{-1}	10.46 %	−0.35	H-cell	[87]
FeNi@7C	NO_3^-	0.1 M KNO_3	1041.33 mmol·h^{-1}·g_{FeNi}^{-1}	15.56 %	−1.2	H-cell	[88]
0.06Bi_2O_3-In_2O_3/Cu_2O	NO_3^-	0.2 M $KHCO_3$ 0.1 M KNO_3	32.59 μmol·h^{-1}·cm^{-2}	39.24%	−0.9	H-cell	[89]
$Cu_3Mo_2O_9$	NO_3^-	0.1 M KNO_3	78.68 mmol·g^{-1}·h^{-1}	26%	−0.8	H-cell	[90]
	NO_3^-	0.1 M KNO_3	177 mmol·g^{-1}·h^{-1}	40%	−0.8	Flow-cell	
F-CNT	NO_3^-	0.1 M KNO_3	6.36 mmol·g^{-1}·h^{-1}	18%	−0.65	H-cell	[91]

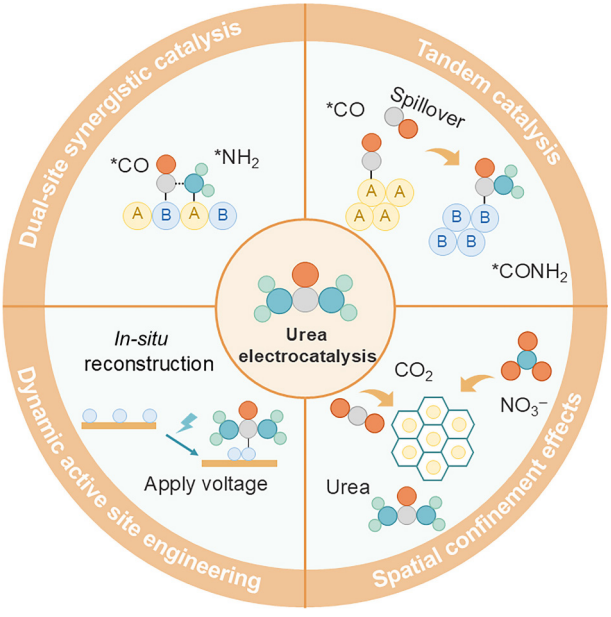

Figure 6 Catalyst design strategies for electrochemical synthesis of urea.

activation. This spatial and functional complementarity synchronizes the otherwise distinct adsorption and reaction kinetics [92, 93]. Moreover, this spatial and functional pairing mitigates the inherent imbalance, where a single active site typically favors one reduction pathway over the other. By co-adsorbing and co-stabilizing key C and N intermediates in close proximity, these proximal sites not only increase the local concentration and encounter probability of the coupling partners but also directly lower the transition-state energy for C–N bond formation. Consequently, this strategy effectively suppresses the independent hydrogenation of each intermediate into side products (e.g., CO, NH_3), thereby steering the reaction network toward selective urea synthesis and alleviating the kinetic competition between CO_2RR and NO_3RR.

Li et al. [27] designed and prepared a $CuWO_4$ catalyst with alternating Cu-W bimetallic sites for the electrocatalytic urea synthesis from CO_2 and NO_3^- (Fig. 7(a)). This catalyst achieved a high urea Faradaic efficiency of 70.1% at a relatively low potential of −0.2 V vs. RHE, corresponding to a urea formation rate of 98.5 $\mu g \cdot h^{-1} \cdot mg_{cat}^{-1}$, which significantly surpasses the performance of the single-component counterparts CuO and WO_3. The high performance originates from a well-defined dual-site synergistic

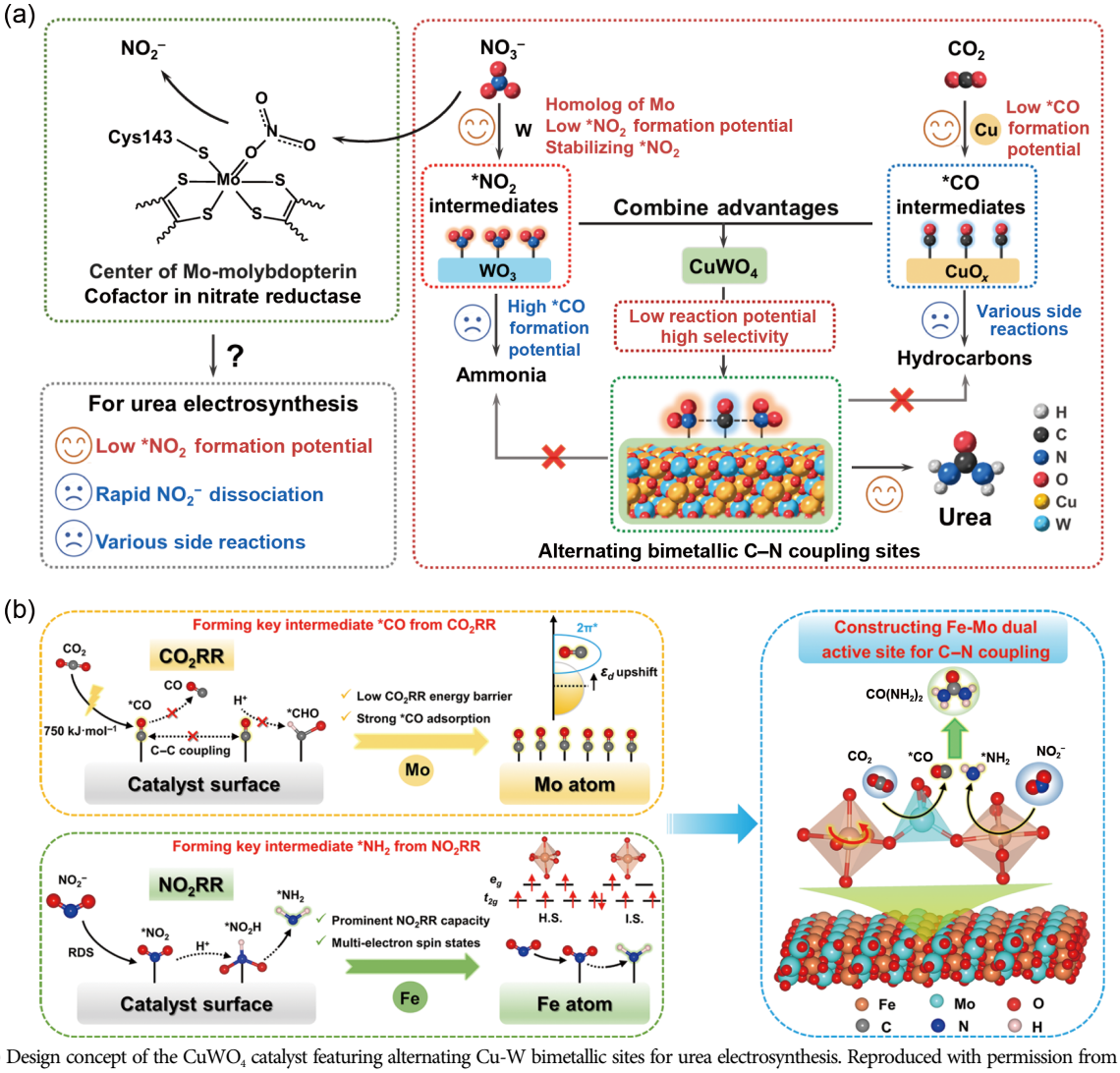

Figure 7 (a) Design concept of the $CuWO_4$ catalyst featuring alternating Cu-W bimetallic sites for urea electrosynthesis. Reproduced with permission from Ref. [27], © Zhao, Y. L. et al. 2023. (b) Schematic illustration of the design strategy for urea electrosynthesis catalyst, highlighting the optimized adsorption of key *CO and $*NH_2$ intermediates on Mo and Fe active sites to facilitate efficient C–N coupling. Reproduced with permission from Ref. [94], © Qian, Q. Z. et al. 2025.

mechanism: The Cu sites are dedicated to activating CO_2 and stabilizing the *CO intermediate, while the adjacent W sites selectively adsorb and stabilize the $*NO_2$ intermediate. This spatially proximate and functionally complementary arrangement of sites enables *CO and $*NO_2$ to efficiently coexist and couple on the catalyst surface, directly forming the C–N bond. *In-situ* Raman spectroscopy and temperature-programmed desorption (TPD) experiments confirmed the co-adsorption and moderate stabilization of both intermediates on $CuWO_4$. DFT calculations further revealed that the reaction-free energy for the coupling of *CO and $*NO_2$ to form $*CONO_2$ (−0.70 eV) is much lower than that for their respective hydrogenation pathways to by-products, thereby thermodynamically steering the reaction toward highly selective urea production. Thus, $CuWO_4$ exemplifies a typical dual-site synergistic catalysis strategy, which effectively promotes C–N coupling through co-stabilization of intermediates and reduction of the energy barrier at adjacent active sites. Xie et al. [94] developed a bimetallic Fe-Mo oxide catalyst (Fe-Mo-O) for electrocatalytic urea synthesis from CO_2 and NO_2^- (Fig. 7(b)). The catalyst exhibits a Faradaic efficiency of 60% and a urea formation rate of 681.8 $\mu g \cdot h^{-1} \cdot mg_{cat}^{-1}$ at −0.5 V vs. RHE, surpassing its monometallic counterparts. This performance is attributed to a dual-site synergistic mechanism: Mo sites selectively adsorb and reduce CO_2 to *CO, while adjacent Fe sites stabilized in an intermediate-spin state (Fe^{3+}) enhance NO_2^- adsorption and conversion to $*NH_2$. The proximity and complementarity of these sites enable *CO and $*NH_2$ to effectively couple into the key urea precursor $*CONH_2$. *In-situ* studies and DFT calculations confirm that the dual-site configuration shifts the d-band center, modulates the Fe spin state, and lowers the energy barrier for C–N coupling. This work demonstrates how the rational design of dual active sites and electronic structure modulation can synergistically facilitate the stabilization of intermediates and the optimization of reaction pathways for selective electrochemical urea synthesis.

Dual-site synergistic catalysis effectively addresses the key challenges of C–N coupling by constructing spatially adjacent and functionally complementary active sites within a single catalyst. Representative examples include $CuWO_4$ and Fe-Mo-O, where paired Cu/W and Mo/Fe sites jointly stabilize and promote the coupling of key intermediates (*CO/$*NO_2$ and *CO/$*NH_2$, respectively). This strategy not only significantly reduces the energy barrier for C–N bond formation but also suppresses side reactions through electronic structure modulation, thereby enabling highly selective and active urea electrosynthesis at low overpotentials. Collectively, these studies indicate that rational design of dual sites and their synergistic interactions offer a promising approach for advancing complex multi-step electrocatalytic reactions toward practical applications.

3.2 Tandem catalysis

Tandem catalysis tackles the kinetic mismatch between CO_2 reduction and NO_3^- reduction by spatially and functionally decoupling the two half-reactions onto distinct active sites. In this design, one site is dedicated to CO_2 activation to form *CO or $*CO_2$, while a separate site selectively reduces NO_3^- to nitrogenous intermediates such as $*NH_2$ or *NO. The carbon intermediate (e.g., *CO) then migrates to the nitrogen-activation site, where C–N coupling occurs in a locally optimized environment. Unlike dual-site synergistic catalysis, which relies on simultaneous intermediate stabilization and coupling at adjacent sites, the tandem catalysis emphasizes step-wise reaction segregation and directed intermediate transport. This sequence can prevent the intrinsic adsorption compromise of single-center catalysts, reduce the kinetic competition between CO_2RR and NO_3RR at the same active site, and alleviate local concentration imbalances. Therefore, tandem catalysis suppresses parallel reduction pathways, minimizes the over-hydrogenation of individual intermediates, and enhances urea selectivity through spatially and temporally coordinated reaction steps.

Li et al. [56] reported a tandem electrocatalytic strategy for urea synthesis using a Pd_2Au_1/RuO_2 catalyst, which spatially decouples CO_2 reduction and NO_3^- reduction. The Pd_2Au_1 sites selectively reduce CO_2 to *CO, while RuO_2 efficiently converts NO_3^- to $*NH_2$. By alloying Pd with Au, the work function difference between Pd_2Au_1 and RuO_2 was minimized to 0.05 eV, thereby suppressing interfacial charge accumulation and promoting remote CO spillover from the metal to the oxide (Fig. 8(a)). Experimental evidence, including CO-TPD and *in-situ* ATR-SEIRAS, confirmed efficient *CO transfer and subsequent coupling with $*NH_2$ on RuO_2. The catalyst achieved a Faradaic efficiency of 75.6% and a urea production rate of 73.5 $mmol \cdot g^{-1} \cdot h^{-1}$ in a flow cell, with an energy consumption of 18.9 $kWh \cdot kg^{-1}$. Sun et al. [43] develop a plasma-electrocatalytic tandem route (pAA-eNCU) for direct urea synthesis from ambient air and CO_2 (Fig. 8(b)). This approach first converts air into highly selective NO_2^- (92.1%) via pulsed high-voltage plasma discharge, followed by electrocatalytic co-reduction of CO_2 and NO_2^- over an oxygen-vacancy-rich single-atom Ru_1/CuO_x catalyst. In the catalyst, Cu-OV sites preferentially activate CO_2 to form *CO, while Ru_1-OV sites selectively reduce NO_2^- to $*NH_2$; subsequent migration of *CO to Ru_1-OV sites enables efficient C–N coupling. The system achieves a urea yield rate of 106.9 $mmol \cdot h^{-1} \cdot g_{cat}^{-1}$ with a Faradaic efficiency of 86.7% at −0.6 V vs. RHE, along with stable operation exceeding 200 h. *In-situ* FTIR and online DEMS confirm key intermediates such as $*CONH_2$, and DFT calculations reveal a low energy barrier for C–N coupling while effectively suppressing competing HER and nitrate reduction. Yu et al. [95] designed a defect-rich CuBi cluster catalyst (D-CuBi) that employs a tandem catalytic strategy to overcome kinetic mismatch in urea electrosynthesis from CO_2 and NO_3^- (Fig. 8(c)). In this system, Cu sites are dedicated to NO_3^- activation and reduction toward *NO, while Bi sites selectively promote CO_2 reduction to *CO. The introduced high-density defects further enhance the functionality of each site: They strengthen CO_2 adsorption on Bi, suppress $*CO_2$ desorption from Cu, and facilitate active water dissociation at the interface. This triple synergistic modulation ensures balanced intermediate supply and efficient coupling of *CO and *NO at the Cu-Bi junction. As a result, D-CuBi achieves a urea Faradaic efficiency of 53.1% and a yield rate of 2.57 $\mu mol \cdot h^{-1} \cdot cm^{-2}$ at −1.0 V vs. RHE, representing a tenfold improvement over the defect-free counterpart. Deng et al. [96] reported a phosphorus-doped Cu/Fe_2O_3 electrocatalyst (P-Cu/Fe_2O_3) for tandem urea electrosynthesis from CO_2 and NO_3^-, in which Cu and Fe sites operate synergistically to activate distinct reactants (Figs. 8(d) and 8(e)). The Cu sites preferentially drive CO_2 reduction to *CO, while the Fe sites facilitate NO_3^- reduction to *NO. Phosphorus doping modulates the electronic structure of the catalyst surface, which not only enhances the formation of *CO and *NO but also lowers the energy barrier for their C–N coupling and promotes *H coverage by facilitating water dissociation, thereby accelerating the hydrogenation steps. This multi-site cooperative

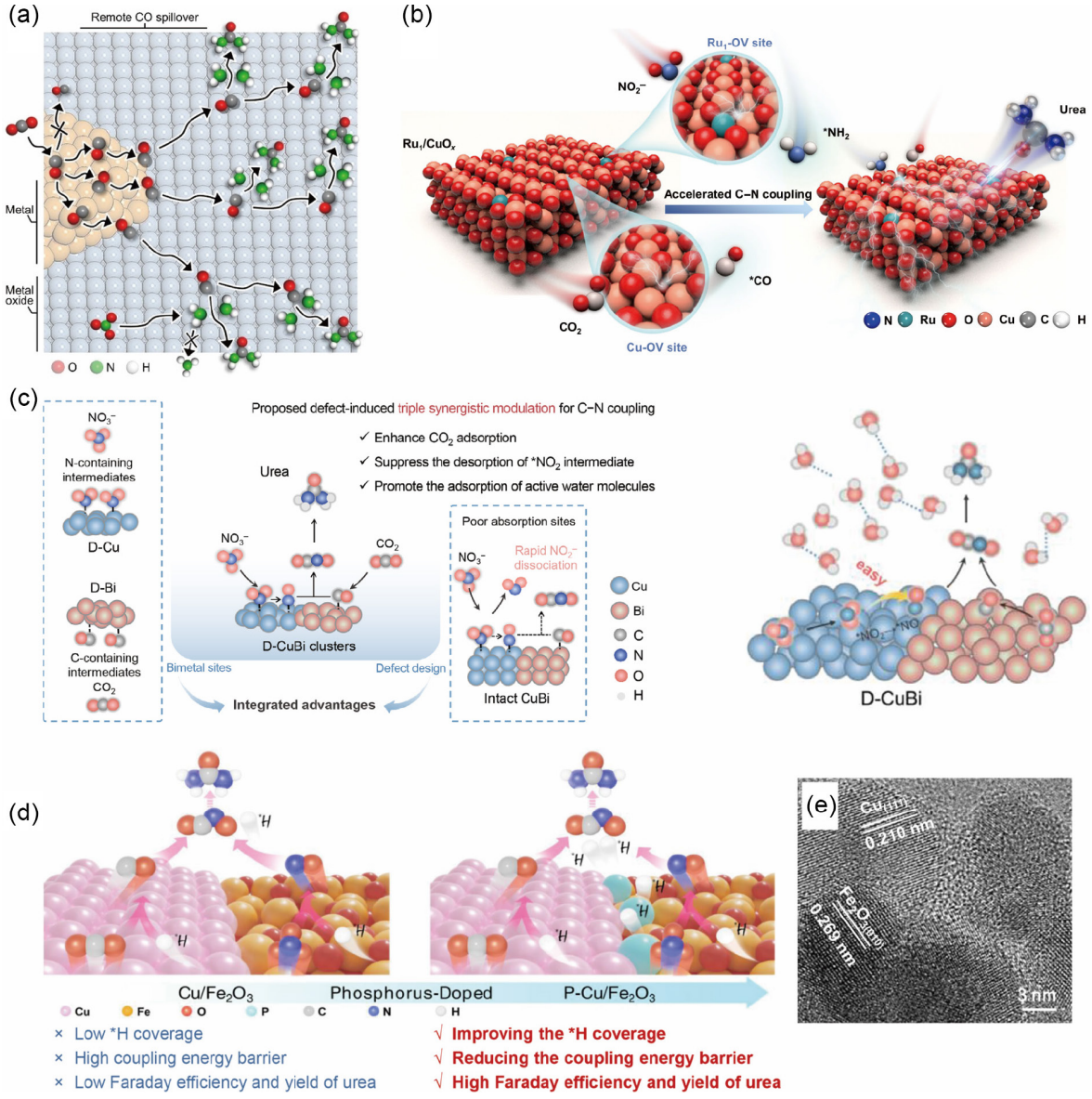

Figure 8 (a) Depicts the catalyst design concept for tandem urea electrosynthesis via remote CO* spillover, featuring the schematic layout, screening of metal and metal oxide components for optimized intermediate generation, and interfacial electronic structure analysis aimed at minimizing the work function difference. Reproduced with permission from Ref. [56], © Wiley-VCH GmbH 2025. (b) Schematic of the eNCU catalysis mechanism on Ru_1/CuO_x. Reproduced with permission from Ref. [43], © Sun, Z. Y. et al. 2025. (c) Schematic representation of the D-CuBi catalyst design for urea electrosynthesis, highlighting the enhanced stabilization of key *CO and *NO intermediates at bimetallic defect sites, which is crucial for efficient C–N coupling. Reproduced with permission from Ref. [95], © Wiley-VCH GmbH 2025. (d) Schematic diagram of the mechanism for C–N coupling process to urea over P-Cu/Fe_2O_3 and Cu/Fe_2O_3. (e) HR-TEM image of P-Cu/Fe_2O_3. Reproduced with permission from Ref. [96], © American Chemical Society 2025.

mechanism enables efficient tandem catalysis, with the P-Cu/Fe_2O_3 catalyst achieving an urea Faradaic efficiency of 73.81% and a yield rate of 62.74 $mmol \cdot h^{-1} \cdot g^{-1}$ at –0.68 V vs. RHE.

3.3 Dynamic active site engineering

Dynamic active site engineering addresses the kinetic mismatch between CO_2 and NO_3^- reduction by enabling the catalytic sites to adapt their structure and electronic state in real time under operating potentials. The disparate reaction pathways and intermediate adsorption requirements for CO_2RR and NO_3RR make it challenging for a static active site to optimally facilitate both processes simultaneously. This strategy overcomes that limitation by allowing the catalyst to undergo reversible structural transformations—such as the dynamic assembly of metal clusters or the change in coordination environment—in response to the applied potential. These transient, reconfigurable sites can be adjusted both electronically and geometrically to alternately stabilize CO_2-derived intermediates (such as *CO) and NO_3^--derived intermediates (such as $*NH_2$, *NO) as the reaction progresses, thereby coordinating the distinct kinetic requirements of the two half-reactions.

Dynamically formed configurations such as Cu_4 clusters exhibit electronic structures that preferentially stabilize the transition state for C–N coupling (Figs. 9(a)–9(c)) [61]. After the reaction ceases, these active sites can reversibly return to their stable ground-state structures, thereby avoiding deactivation associated with long-term

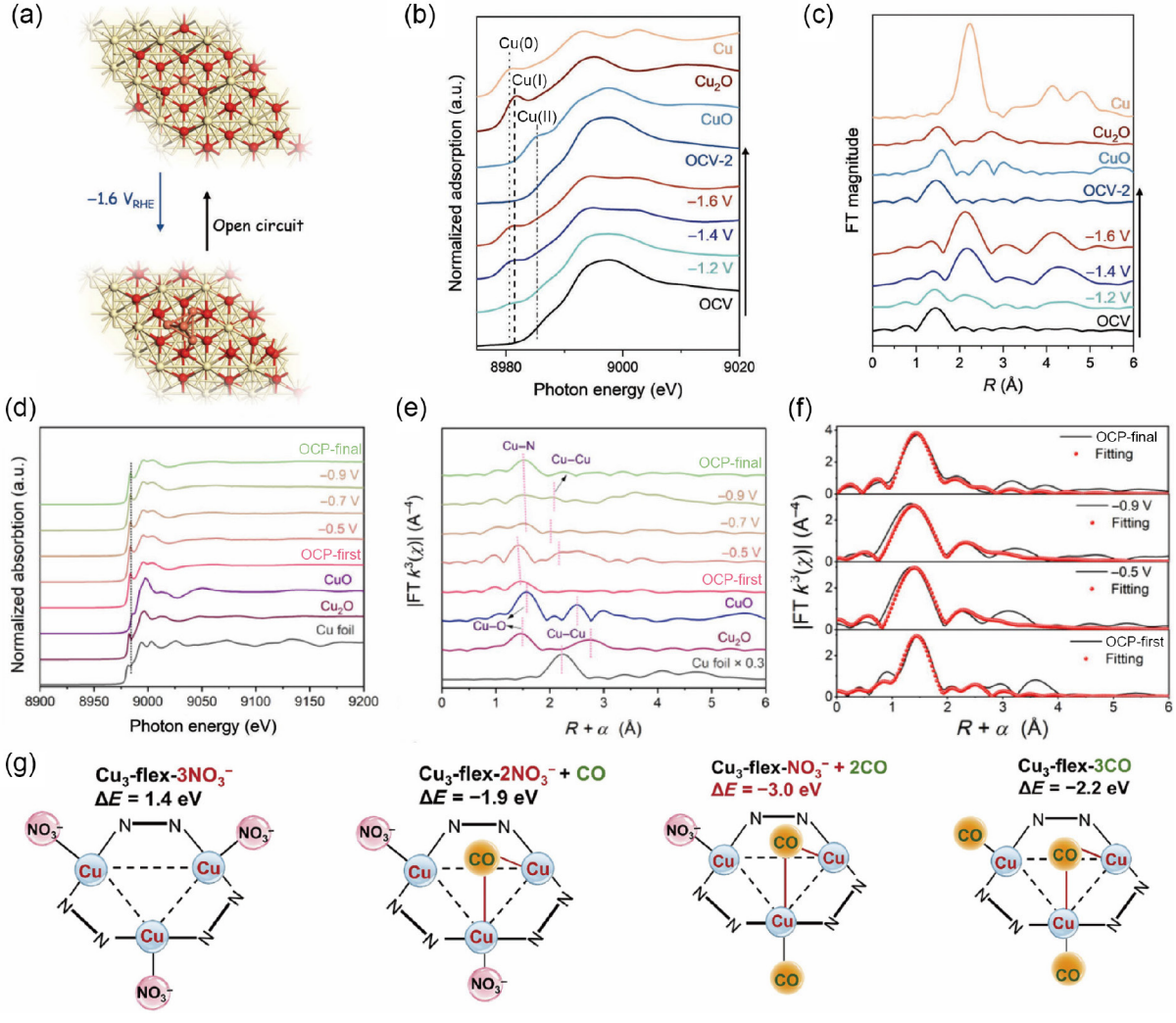

Figure 9 (a) *In-situ* XAS analysis reveals the dynamic transformation of copper single atoms into clusters during the electrocatalytic process. (b) The Cu K-edge XANES spectra of Cu_1-CeO_2, collected under progressively increasing cathodic potentials, reflect changes in the electronic structure and local coordination of Cu species throughout the C–N coupling reaction. (c) Corresponding *R*-space EXAFS spectra further illustrate the evolution of Cu–Cu scattering paths, confirming the potential-driven aggregation of atomic Cu into clustered motifs. Reproduced with permission from Ref. [61], © Wiley-VCH GmbH 2023. (d) *In-situ* Cu K-edge XANES, (e) k^3-weighted FT-EXAFS and (f) Cu K-edge EXAFS fitting curves spectra of Cu-N_3 SAs recorded under various potentials during electrochemical urea synthesis. Reproduced with permission from Ref. [72], © Wiley-VCH GmbH 2025. (g) Energy changes for the adsorption of $3NO_3^-$, $3NO_3^-$ + CO, NO_3^- + 2CO, and 3CO on a Cu_3-flex molecule. Reproduced with permission from Ref. [97], © American Chemical Society 2025.

metastable high-energy states. This approach thereby combines enhanced catalytic selectivity with improved operational stability. Thus, dynamic active site engineering provides an adaptive, potential-driven route to synchronize the kinetically distinct CO_2 and NO_3^- activation steps, leading to more efficient and selective urea formation.

Liu et al. [72] developed a g-C_3N_4-supported Cu-N_3 single-atom catalyst (Cu-N_3 SAS) for electrocatalytic urea synthesis from CO_2 and NO_3^-, achieving a high urea yield rate of 19,597.65 ± 1821.24 $\mu g \cdot h^{-1} \cdot mg_{Cu}^{-1}$ and a Faradaic efficiency of 55.4% ± 1.89% at −0.9 V vs. RHE. The key mechanism involves the reversible dynamic reconstruction of active sites under operating potential. *In-situ* X-ray absorption spectroscopy (XAS) directly revealed the isolated Cu-N_3 coordination restructures into N_2-Cu-Cu-N_2 dual-sites upon applying potentials of −0.5 V and above, accompanied by Cu–N bond breaking and new Cu–Cu bond formation; this reconstructed configuration reversibly reverts to the initial Cu-N_3 state when the potential is removed (Figs. 9(d)–9(f)). The *in-situ* generated dynamic dual-site structure is central to the enhanced catalytic performance. Intermediate-monitoring experiments further elucidated its role: *operando* ATR-SEIRAS detected *CO adsorption at ~ 1836 cm^{-1} and C–N vibration at ~ 1456 cm^{-1}, while DEMS directly captured the signal of the key C–N coupling intermediate *CONH (m/z = 43), confirming the reaction pathway *CO + *NH → *CONH. Theoretical calculations demonstrated that, compared to the static Cu single-atom/cluster structure (Cu SAs/ACs-N), the dynamically formed N_2-Cu-Cu-N_2 sites significantly strengthen *CO adsorption (desorption free energy 1.0 vs. 0.48 eV) and lower the energy barrier for *CO and *NH coupling to *CONH from 0.9 to 0.7 eV, thereby cooperatively promoting efficient C–N bond formation both thermodynamically and kinetically. By correlating *in-situ* structural characterization, intermediate tracking, and theoretical modeling, this work provides a complete demonstration of a new catalytic paradigm in which

potential-driven dynamic active-site reconstruction optimizes intermediate stabilization, reduces the C–N coupling barrier, and enables highly efficient urea synthesis.

Xu et al. [97] reported a trinuclear copper molecular catalyst (Cu_3-flex) featuring triangular Cu_3 sites with dynamically adaptive inter-copper spacings for electrocatalytic urea synthesis from CO_2 and NO_3^-. The catalyst delivered a urea production rate of 122 ± 8 mmol·g_{cat}^{-1}·h^{-1} and a Faradaic efficiency of 69% ± 4.0% at −0.6 V vs. RHE. The high performance originates from the dynamic self-adjustment of the active-site structure during reaction. *In-situ* XAS revealed that under electrolysis conditions, part of the Cu–Cu distances shortened from ~ 3.4 to 2.4–2.5 Å. Combined with the shifts of vibrational peaks observed by *in-situ* Raman spectroscopy (Fig. 9(g)), these results confirm the dynamic changes in the coordination environment of the catalyst. This structural flexibility enables the optimal co-adsorption of reaction intermediates: Theoretical calculations identified the most stable configuration as the adsorption of one *NO_3^- and two *CO (ΔE = −3.0 eV), in which one *CO adopts a bridging mode between two Cu sites, directly reducing the inter-copper distance, consistent with experimental observations. The dynamically shortened Cu–Cu spacing not only facilitates the first C–N coupling of *CO and *N to form the key *NCO intermediate (with a further lowered ΔG), but also creates a favorable geometric and electronic environment for the subsequent adsorption of a second *NO_3^- and the second C–N coupling Gibbs free-energy profiling of the entire reaction pathway showed that both C–N coupling steps are thermodynamically spontaneous (ΔG < 0) on Cu_3-flex, whereas the reference catalyst Cu_3-rigid, lacking such dynamic structural adaptability, exhibits significantly higher energy barriers for C–N coupling. Thus, this work elucidates a new mechanism in which dynamic structural self-adaptation of catalyst active sites optimizes the adsorption geometry and distance of intermediates, thereby substantially lowering the energy barriers for multi-step C–N coupling reactions.

In addition to the description of the dynamic reconstruction phenomenon, it is also necessary to understand the fundamental driving forces that govern this structural evolution under operating conditions. From a theoretical perspective, there are two interrelated factors that play a decisive role:

(i) The external operating potential for electrocatalytic urea synthesis serves as an energy input, altering the electron distribution at the active centers of the catalyst and the bond energy of chemical bonds, triggering the breakage of coordination bonds and the formation of new bonds, and driving reversible structural rearrangements at the active sites [62, 72].

(ii) The different intermediates produced by the reduction of CO_2 and NO_3^- will induce dynamic changes in the structure and electronic state of the catalyst's active sites, in order to adapt to the adsorption, activation and C–N coupling requirements for various intermediates [97].

This indicates that dynamic reconfiguration is not merely a passive response to potential situations, but rather an active, thermodynamic-driven process that optimizes the electronic and geometric structures of the catalyst based on the current reaction conditions. By combining theoretical research and *in-situ* spectroscopic studies to understand these driving factors, it is crucial for the rational design of adaptive catalysts that can dynamically reconfigure to meet the constantly changing requirements of multi-step C–N bond formation reactions.

Current literature confirms that potential-driven dynamic restructuring can optimize C–N coupling; however, research still primarily focuses on Cu-centric, with limited real-time mechanistic insights and general design principles. Advancing this field requires combining *operando* techniques with higher spatiotemporal resolution and machine learning-augmented simulations to accurately track and predict active site dynamics. Future research directions should extend to non-copper and multi-metal systems and explore external field (e.g., light, heat) coupling to design adaptive catalysts that simultaneously achieve high activity, selectivity, and durability.

3.4 Spatial confinement effects

The spatial confinement effect offers an effective strategy to mitigate the kinetic imbalance between CO_2 and NO_3^- reduction by creating tailored nanoreactors, while simultaneously addressing their mismatched diffusion rates, local concentrations, and intermediate adsorption behaviors. The inherent differences between gaseous CO_2 diffusing slowly toward the catalyst surface and aqueous NO_3^- ions rapidly approaching the catalyst surface typically result in an excess of local nitrogen intermediates and a shortage of carbon intermediates, thereby favoring the independent reduction of NO_3^- rather than C–N coupling. By leveraging the well-defined pores and channels of materials such as metal-organic frameworks (MOFs), covalent organic frameworks (COFs), and hollow multi-shelled structure (HoMS), confinement architectures can co-trap and concentrate both CO_2 and NO_3^- within the same nanoscale space [98–102]. This forced proximity dramatically increases the local concentration and collision frequency of their respective intermediates (e.g., *CO from CO_2 and *NH_2/NO_2 from NO_3^-), effectively compensating for the diffusion-limited supply of CO_2. Spatial confinement not only alleviates the reactant-supply imbalance but also creates a microenvironment where the kinetics of CO_2 and NO_3^- activation are harmonized, thereby enhancing the selectivity and yield of urea electrosynthesis.

Regulating the spatial distance of the layered structure to match the geometric dimensions of the reaction intermediates and urea promotes C–N coupling. Zhang et al. [73] designed layered copper polyphthalocyanine (CuPPc) catalysts with tunable interlayer spacings (4.0, 4.6, and 5.7 Å) to function as "interlayer dual-atom molecular reactors" for urea electrosynthesis from CO_2 and NO_3^- (Figs. 10(a)–10(c)). The optimized CuPPc-4.0 with a 4.0 Å spacing achieved a urea yield rate of 460.0 mmol·h^{-1}·g^{-1}, a Faradaic efficiency of 26.1%, and a partial current density of 42.6 mA·cm^{-2} at −1.3 V vs. RHE, significantly outperforming its wider-spaced counterparts. The exceptional performance stems from a geometric confinement effect: The 4.0 Å cavity closely matches the molecular dimension of urea (~ 3.5 Å), spatially aligning key intermediates such as *$CONH_2$ and *NH_2CONO to promote C–N coupling. Paired, non-bonded interlayer Cu-N_4 sites, confirmed by extended X-ray absorption fine structure (EXAFS) and wavelet transform analysis, co-adsorb and activate *CO and *NH_2 intermediates, as detected by online DEMS (m/z = 44, 45). DFT calculations reveal that the 4.0 Å confinement provides the lowest free-energy barrier for *$CONH_2$ formation (ΔG = −1.40 eV) and for the subsequent hydrogenation of *NH_2CONOH (+0.29 eV), thermodynamically steering the reaction toward urea. This underscores that intact layer stacking and precise spatial matching, rather than merely maximizing active-site exposure, are critical for efficient C–N coupling. The work demonstrates a strategy that integrates geometric confinement with dual-site synergy to direct complex electrocatalytic reactions. The spatial

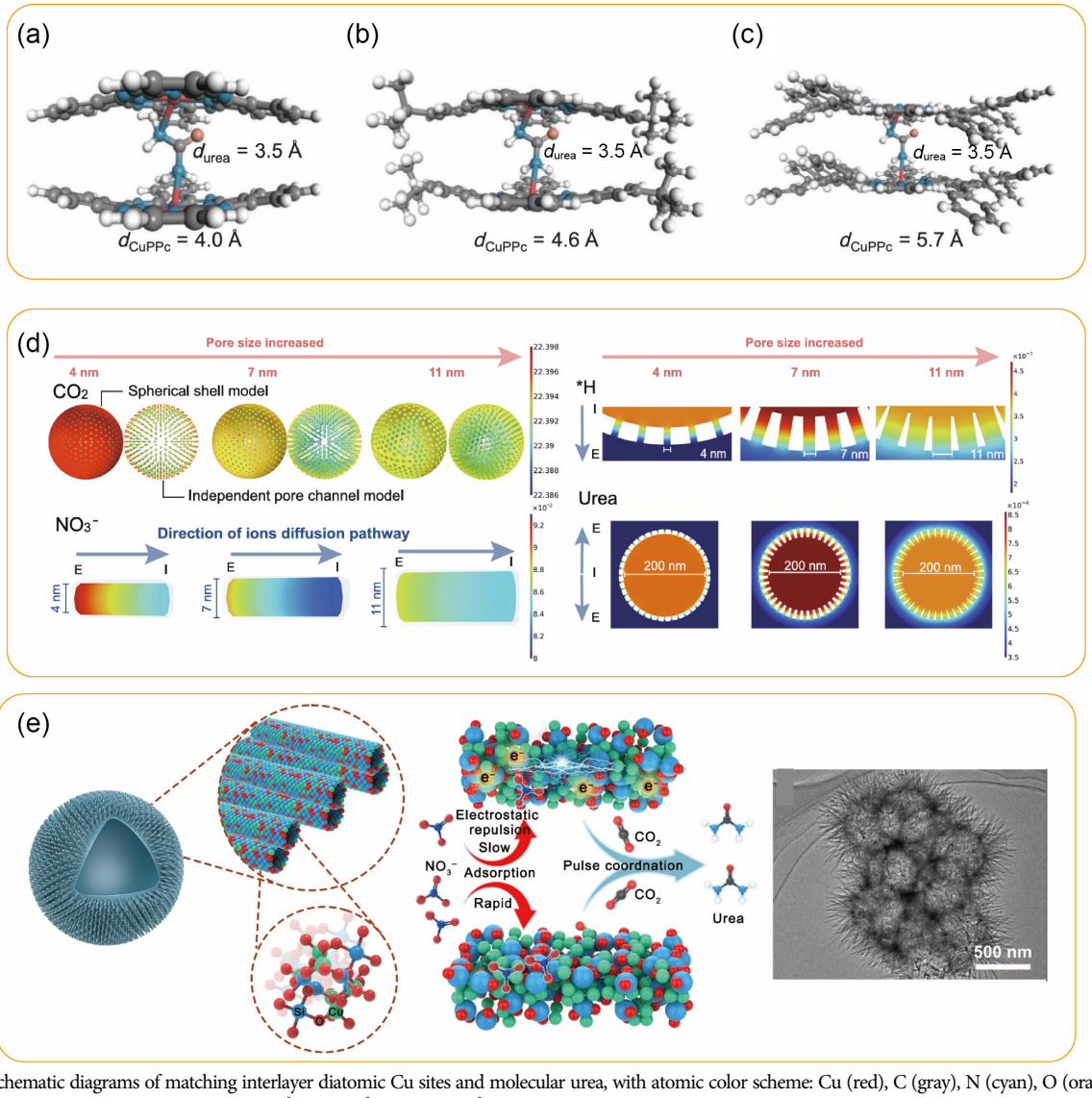

Figure 10 Schematic diagrams of matching interlayer diatomic Cu sites and molecular urea, with atomic color scheme: Cu (red), C (gray), N (cyan), O (orange), and H (white) for CuPPc with interlayer space of (a) 4.0 Å, (b) 4.6 Å, and (c) 5.7 Å, respectively. Reproduced with permission from Ref. [73], © Wiley-VCH GmbH 2025. (d) Computed concentration and distribution of species: CO_2, NO_3^-, *H and urea concentration. Three dimensional MCHS with precisely tuned pore diameters (4, 7, and 11 nm) and a 2 nm catalytic layer were constructed to match with the structural features of CuRu/MCHS catalysts. Reproduced with permission from Ref. [103], © Du, J. X. et al. 2025 (e) Schematic diagram of $CuSiO_x$ structure and pulse enhanced electrocatalytic coupling of CO_2 and nitrate to synthesize urea. Reproduced with permission from Ref. [85], © Wiley-VCH GmbH 2024.

confinement effect of MOF is mainly manifested as follows: Through its regular nanochannels, it physically restricts the catalytic species of the guest and regulates the chemical microenvironment. This confinement effect not only prevents the aggregation of active nanoparticles and enables their uniform dispersion in an ultra-small size, but also enriches the reaction intermediates and precisely regulates their adsorption energy and stability. Huang et al. [64] encapsulated ultrasmall γ-Fe_2O_3 nanoparticles (< 2 nm) within the one-dimensional nanochannels (~ 2 nm diameter) of a conductive Ni-HITP MOF, constructing a γ-Fe_2O_3@Ni-HITP catalyst for electrocatalytic urea synthesis from CO_2 and NO_3^-. At −0.8 V vs. RHE, the catalyst achieved a urea Faradaic efficiency of 67.2% and a remarkably high yield rate of 20.4 $g \cdot h^{-1} \cdot g_{cat}^{-1}$. The exceptional performance is attributed to the spatial confinement provided by the MOF channels. This confinement effectively stabilizes the γ-Fe_2O_3 nanoparticles against aggregation and ensures their uniform dispersion, thereby exposing abundant active sites. DFT calculations reveal that the confined di-iron sites favor the direct coupling of *COOH and *NH_2 (ΔG = −1.07 eV) over the further hydrogenation of *COOH to formate (ΔG = +0.45 eV). The MOF's nanochannels thus not only enrich key intermediates but also fine-tune their stability, steering the pathway toward selective C–N coupling while suppressing side reactions. This confinement-driven mechanism underlies the catalyst's high activity, selectivity, and long-term stability (> 150 h) in urea electrosynthesis. The hollow structure creates a customized nano-reactor microenvironment, which can facilitate the enrichment of reactants and stabilize key intermediate products, fundamentally altering the pathway of carbon-nitrogen coupling. Zhang et al. [103] (Fig. 10(d)) designed a nano-confined CuRu bimetallic catalyst embedded within mesoporous carbon hollow spheres (CuRu/MCHS) to address kinetic and mass-transport limitations in urea electrosynthesis from CO_2 and NO_3^-. The spatially confined architecture, with precisely engineered pore channels (~ 7 nm), creates a microenvironment

that enriches reactants and stabilizes key intermediates. *In-situ* spectroscopy and theoretical calculations reveal that the nano-confinement shifts the dominant C–N coupling pathway from the conventional COOH-NH_2 route to a kinetically favored OCO–NO coupling, bypassing high-energy hydrogenation steps. The confined space also enhances the retention and utilization of active hydrogen (*H), directing it toward selective hydrogenation in the urea-forming pathway rather than toward H_2 evolution. As a result, CuRu/MCHS achieves a high urea yield rate of 12.51 $g \cdot h^{-1} \cdot g_{cat}^{-1}$ at an industrially relevant current density of 250 $mA \cdot cm^{-2}$, along with stable operation over 125 h. Qiu et al. [85] utilized the spatial confinement of $CuSiO_x$ nanotubes with abundant atomic Cu-O-Si interfacial sites to create a stable microenvironment that enriches *CO and *NO_2 intermediates and promotes their direct C–N coupling, thereby enhancing urea selectivity and stabilizing the active sites against reconstruction (Fig. 10(e)).

The spatial confinement effect enhances urea synthesis by leveraging nanospaces to enrich reactants and direct the alignment of key intermediates, thereby promoting selective C–N coupling. Current research primarily focuses on confinement at the nanoscale and sub-nanoscale, while precise geometric control over the catalyst's structure remains insufficient. The cited studies demonstrate that tuning pore dimensions or interlayer spacing can spatially arrange and activate critical intermediates, significantly improving reaction selectivity and efficiency. Therefore, gaining a deeper understanding of the relationship between the geometry of confined spaces and catalytic performance is a critical area for future catalyst design [104–108].

3.5 The synergistic role of catalyst supports

Apart from the design of the active sites, the catalyst carrier also plays an equally important role in determining the electrocatalytic performance. This carrier not only can disperse and stabilize the active substances, but also can actively regulate their electronic structure and directly participate in the reaction mechanism.

Firstly, the aggregation phenomenon is prevented by anchoring the active site. Nitrogen-doped carbon stabilizes the Cu single atoms through Cu-N_x coordination, and the configuration of nitrogen affects the binding strength and oxidation state of the metal [44, 72]. Secondly, the electronic properties are regulated through the interaction between metal and the carrier. In γ-Fe_2O_3@Ni-HITP [64], the conductive metal-organic framework promotes the transfer of electrons to the Fe sites, thereby optimizing the adsorption of *COOH and *NH_2. Thirdly, the carrier can actively participate in the cooperative catalytic process. In Cu/ZnO [42], ZnO selectively converts CO_2 into *CO, and then this substance migrates to the Cu site to combine with *NH_2. Finally, the structure of the carrier forms a confined microenvironment, such as high-porosity metal structures [101], metal-organic frameworks [64], and mesoporous carbon [103], which can increase the content of reactants and stabilize intermediate products.

Therefore, the catalyst carrier is an indispensable component. It can be designed rationally to stabilize the active sites, adjust their electronic properties, and create a favorable reaction environment for efficient C–N coupling.

3.6 Other strategies

In addition to the core design paradigm, several auxiliary strategies have been developed to further enhance electrocatalytic urea synthesis by addressing secondary performance determinants. The electronic interactions between active components and functional supports (such as conductive oxides or frameworks) can also be engineered to improve charge transfer and stabilize active species, as observed in systems where the support actively participates in intermediate formation [109]. Altering the local chemical environment at the electrode–electrolyte interface is another effective approach. For example, through hydrophobic/polymer bilayer coatings, the concentration of reactants (CO_2) can be increased while suppressing competing reactions such as HER, thereby enhancing the selectivity for urea production [110]. Finally, going beyond conventional slurry-casting methods, *in-situ* catalyst growth techniques (e.g., electrodeposition) can be directly integrated onto the substrate without binders, thereby enhancing active site exposure, electrical contact, and durability under high-current-density operation [111]. Overall, these strategies provide complementary levers for fine-tuning catalyst performance and system integration, contributing to multifaceted advances in electrochemical urea synthesis.

In addition to promoting the C–N coupling reaction, consideration must also be given to the issue of intermediate poisoning under continuous operation conditions. Strongly adsorbed substances, such as *CO or N-containing intermediates (such as *NO, NH_x), may accumulate at the active sites and hinder further substrate adsorption, thereby leading to catalyst deactivation and reduced urea production. Several strategies have been developed to mitigate this poisoning effect: (i) surface engineering to modulate adsorption strength: Tuning the electronic structure of active sites via doping or alloying can optimize the adsorption energy of key intermediates, preventing overly strong binding that leads to site blockage. For example, the interface electron regulation of CoPc-COF@TiO_2 nanoparticles can alter the adsorption conditions of *CO and *NH_2 intermediates, thereby enabling efficient C–N coupling reactions during urea synthesis [109]. (ii) Tandem catalyst aims to achieve spatial separation of intermediate products: By confining the reduction of CO_2 and the reduction of NO_3^- to different, spatially independent sites, tandem catalysis can minimize the competitive adsorption of different intermediate products at the same site, thereby reducing the risk of poisoning [56, 95]. (iii) Dynamic active site evolution: Catalysts that undergo reversible structural transformations under operating potentials can periodically release strongly bound intermediates, as demonstrated by the dynamic Cu cluster formation reported by Liu et al. [72], where potential-driven reconstruction prevents permanent site occupation. (iv) Design of confined micro-environment: HoMS and MOF nano-channels not only increase the amount of reactants, but also promote the desorption of products and intermediates by providing alternative diffusion paths, thereby reducing the accumulation of harmful substances in local areas [103].

4 Electrolyte and reactor engineering: optimizing the reaction microenvironment

4.1 Electrolyte engineering

Beyond the catalyst itself, the microenvironment in which the reaction occurs, including the composition of the electrolyte and the configuration of the reactor, plays an equally important role in determining the performance of urea electro-synthesis [13, 112, 113]. Optimizing the electrolyte and the reactor to improve quality

transfer, interfacial electric field, and local reactant concentration is a key complementary strategy for increasing the yield and selectivity of urea. This chapter explores how systematic improvements to the reaction microenvironment through electrolyte formulation and advanced reactor design can overcome inherent limitations and guide the complex carbon-nitrogen coupling network towards efficient production of urea.

In electrocatalysis, tailoring the electrolyte composition is a well-established strategy to modulate reaction kinetics, intermediate stabilization, and product selectivity. For instance, in the CO_2RR, extensive electrolyte engineering—including cation effects, pH control, anion selection, and the use of organic additives—has been crucial for enhancing the efficiency and selectivity toward valuable C_1 and C_{2+} products [114–120]. In contrast, electrolyte optimization for electrocatalytic urea synthesis from CO_2 and NO_3^- remains in its infancy, with research to date predominantly focused on the role of alkali metal cations. This section therefore centers on the cation effect as the most explored electrolyte parameter in urea electrosynthesis, while acknowledging that broader electrolyte design space awaits systematic investigation.

The cations in the electrolyte, especially the alkali metal cations, not only act as charge carriers but also specifically adsorb onto the negatively charged electrode surface, forming an electric double layer structure. Larger cations, such as K^+ and Cs^+, have relatively loose hydration layers, allowing them to be closer to the electrode surface and accumulate on the Helmholtz plane, enhancing the local electric field. This enhanced electric field effectively reduces the repulsion between negatively charged C/N intermediates through electrostatic stabilization, promoting their enrichment and aggregation in space, thereby significantly lowering the activation energy barrier for C–N coupling and facilitating the formation of key intermediates (such as *ONCO) [121–124].

Currently, in the research on electrochemical C–N bond formation for urea synthesis, it has been found that the effect of cations influences the selectivity and activity of the reaction. Research shows that the promotional effect of different alkali metal cations on urea formation follows the trend $Li^+ < Na^+ < K^+$, with K^+ performing the best. For example, under constant potential electrolysis in a pure potassium nitrate electrolyte (0.1 M KNO_3) at -0.3 V vs. RHE, a urea Faradaic efficiency of 30.8% and a current density of 181 $\mu A \cdot cm^{-2}$ were achieved (Fig. 11(a)) [125]. In contrast, adding crown ether (18-crown-6) to chelate K^+ significantly reduced urea yield (Figs. 11(b) and 11(c)), indicating that free cations are crucial for promoting the reaction. Theoretical analysis suggests that larger cations such as K^+ and Cs^+ possess softer hydration shells, which more effectively shield the Coulombic repulsion between nitrate anions and the negatively charged electrode, thereby promoting the adsorption and activation of NO_3^- on the electrode surface. However, although Cs^+ performs well in traditional CO_2 reduction reactions, in C–N coupling it forms an overly compact double layer that hinders NO_3^- mass transport, leading to lower urea selectivity. Tu et al. [46] systematically investigated the effect of alkali metal cations (Li^+, Na^+, K^+, Cs^+) on electrocatalytic urea synthesis, revealing a urea yield trend of $Li^+ < Na^+ < Cs^+ < K^+$ (Figs. 11(d) and 11(e)). In the presence of 1.0 M K^+, a high urea yield rate of 265.6 ± 13.3 $mmol \cdot h^{-1} \cdot g^{-1}$ was achieved on a TiO_2 catalyst at −1.50 V vs. RHE, with K^+ significantly enhancing the signal intensity of the key coupling intermediate *ONCO (Fig. 11(f)). *Operando* SR-FTIR combined with isotopic labeling experiments (using $^{15}NO_3^-$) confirmed that K^+ stabilizes the negatively charged *CO and *NO intermediates via electrostatic interactions, promoting their enrichment and assembly at the electrode/electrolyte interface. This reduces the kinetic barrier of C–N coupling to 0.22 eV (Fig. 11(g)), which is much lower than those for Li^+ (0.73 eV) and Na^+ (0.61 eV). These results collectively demonstrate that K^+ not only facilitates reactant transport through electrostatic shielding but also significantly lowers the reaction energy barrier by stabilizing coupling intermediates, establishing it as the key cation for achieving efficient electrochemical C–N coupling.

Looking forward, there are several electrolyte parameters that have not been thoroughly studied and are worthy of systematic research in order to further advance the electrochemical synthesis process of urea. The type and concentration of anions can significantly affect the electric double layer structure, the local pH value, and the intermediate stable state [114, 115]. However, their role in the mechanism of C–N coupling remains unknown. The local pH modulation, whether through buffer capacity tuning or pulsed electrolysis, offers a promising lever to control proton availability and suppress competing hydrogenation reactions. Organic additives and ionic liquids, which have shown remarkable ability to stabilize key intermediates and alter reaction pathways in CO_2RR, remain virtually unexplored in the context of urea synthesis [118, 119]. Furthermore, the interaction between the electrolyte composition and the surface structure of the catalyst needs to be established through comprehensive *in-situ* characterization and theoretical modeling to establish a predictable structure–activity relationship. The systematic exploration of these multi-dimensional electrolyte variables is expected to open up new fields for the selectivity and activity in electrochemical C–N bond formation reactions.

4.2 Reactor engineering for optimizing the reaction microenvironment

From the perspective of reactor design, traditional H-cells are limited by the transport of gas reactants (such as CO_2). In H-cell, CO_2 must first dissolve in the electrolyte before it can diffuse onto the catalyst surface, which results in a lower local concentration of CO_2 and limited current density, especially in cases of high reaction rates. Transitioning to flow-cell equipped with GDEs is a key breakthrough to address this bottleneck. In the flow-cell, CO_2 is directly supplied to the backside of the porous and hydrophobic GDE, while the electrolyte flows on the front side coated with the catalyst (Figs. 12(a) and 12(b)). This configuration establishes a stable gas–liquid–solid three-phase interface, allowing CO_2 to directly reach the catalytic site without the need for prior dissolution.

This reactor optimization has significantly enhanced the performance of urea electrosynthesis across various catalytic systems. For instance, γ-Fe_2O_3@Ni-HITP in a flow-cell achieved a current density of −90 $mA \cdot cm^{-2}$ and a urea production rate of 20.4 $g \cdot h^{-1} \cdot g_{cat}^{-1}$ outperforming most H-cell systems by more than an order of magnitude, while maintaining stable operation for over 150 h and enabling gram-scale urea synthesis [64]. Similarly, using the TiO_2-C catalyst, the urea production rate increased from 19.53 $mmol \cdot g^{-1} \cdot h^{-1}$ in an H-cell to 43.37 $mmol \cdot g^{-1} \cdot h^{-1}$ in a flow-cell, with the Faradaic efficiency improving from 45.14% to 48.88% [60]. These results consistently demonstrate that the flow-cell configuration, by enhancing CO_2 mass transport and surface supply, substantially increases the reaction rate while preserving

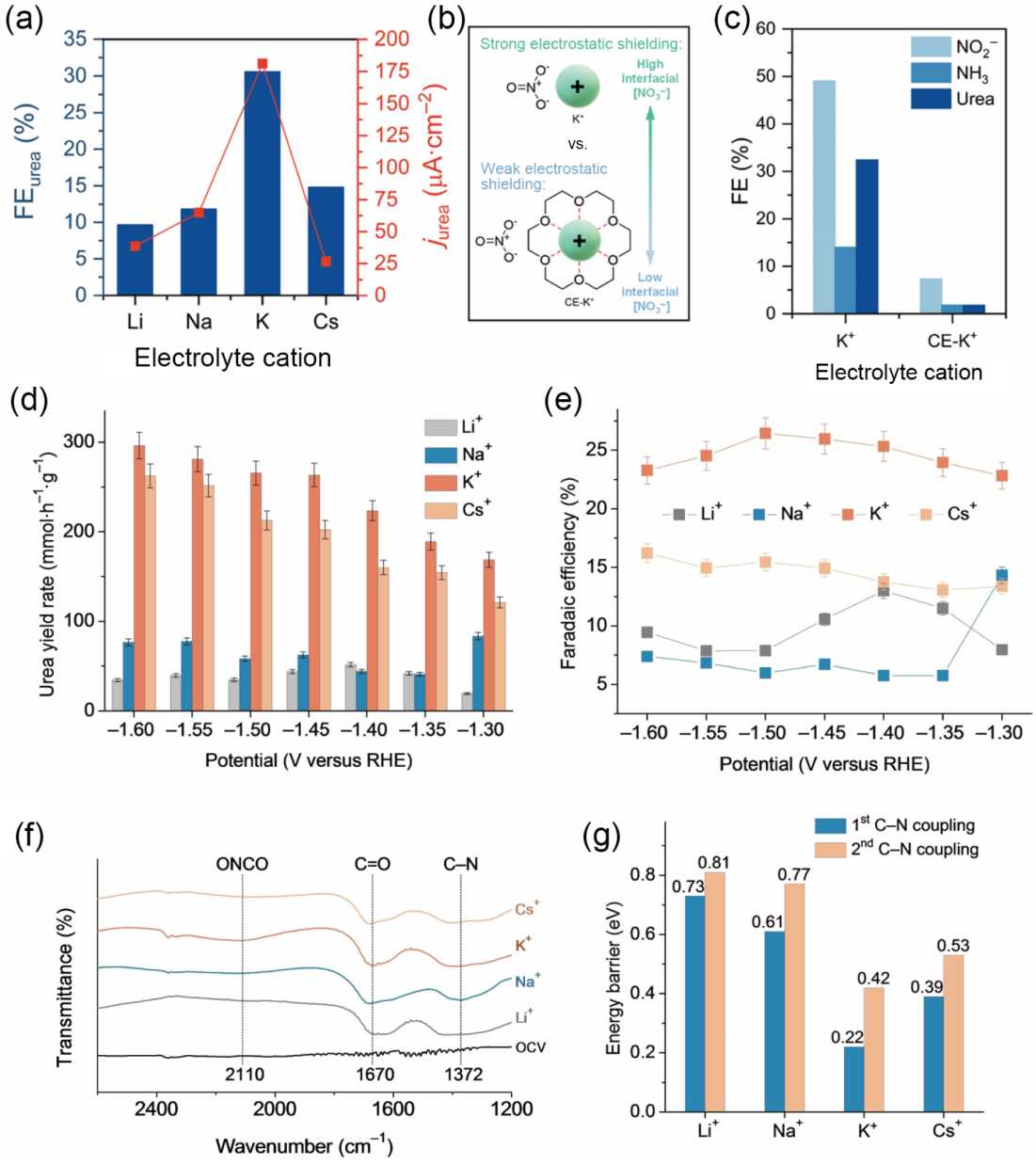

Figure 11 (a) Electrolyte cation optimization in 0.1 M XNO_3 (X = Li, Na, K or Cs) at pH 3 from constant potential electrolysis at −0.3 V vs. RHE. (b) Scheme representing the role of electrolyte cations on nitrate reduction as free or chelated ions. (c) Liquid products following electrolysis under a constant purge of CO_2 at −0.3 V vs. RHE in the absence and presence of 18-crown-6ether (CE-K$^+$, 1.1 equiv to K$^+$). Reproduced with permission from Ref. [125], © American Chemical Society 2023. (d) Urea yield rates and (e) corresponding Faradaic efficiencies in electrolytes containing 1.0 M of Li$^+$, Na$^+$, K$^+$, and Cs$^+$ at −1.50 V ions under various applied potentials, respectively. (f) Infrared signal in the range of 1200–2600 cm^{-1} at 1.5 V vs. RHE during co-electrolysis in electrolytes containing 1.0 M of various cations. (g) Kinetic C–N coupling barrier. Reproduced with permission from Ref. [46], © Wiley-VCH GmbH 2023.

high selectivity, thereby providing a crucial reactor-engineering foundation for advancing urea electrosynthesis toward practical application.

In addition to performance improvement, the design of the reactor fundamentally affects the rate of the C–N coupling reaction through three key mechanisms: (i) enhanced CO_2 material transport: The flow-cell with gas diffusion electrodes can directly transport gaseous CO_2 to the catalyst surface, significantly increasing the local coverage of CO_2. This enables the CO_2RR and NO_3RR reactions to reach a kinetic balance, overcoming the inherent defect where there is a tendency to prefer NO_3^- reduction alone rather than C–N coupling due to concentration differences [126, 127]. (ii) Local micro-environment control: Continuous electrolyte flow can better regulate the local pH value and reactant concentration compared to H-cell. By optimizing the flow rate and electrolyte composition, the pH value at the interface can be maintained, thereby balancing the proton supply for urea formation and simultaneously inhibiting the competing hydrogen evolution reaction, reducing the barrier for C–N coupling [122, 123].

From the perspective of reactor design, transitioning from the traditional H-cell to the flow-cell significantly overcomes the intrinsic mass-transport limitations for gaseous CO_2, enabling higher current density and urea production while maintaining good selectivity. However, the application of flow-cell in urea

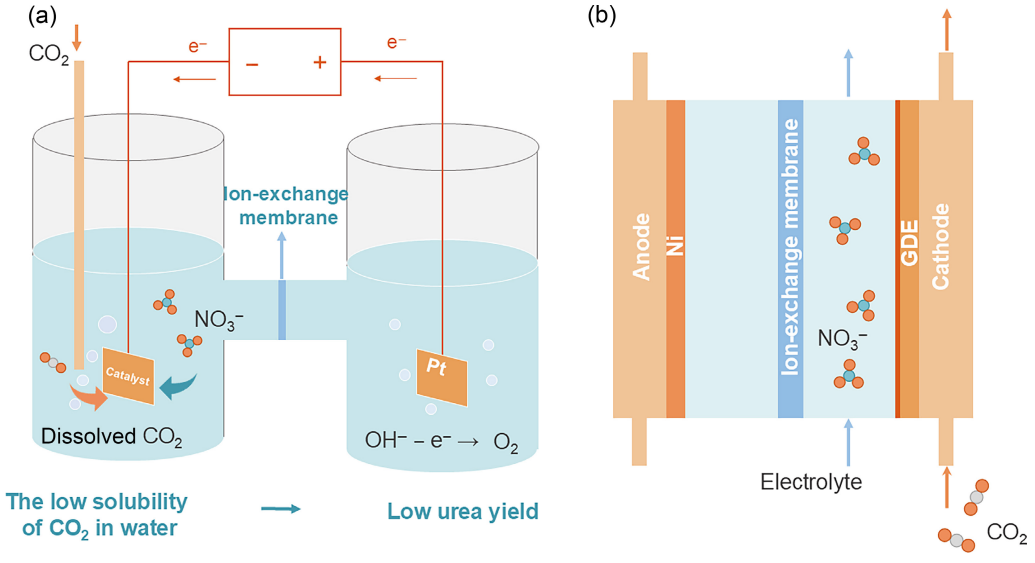

Figure 12 Schematic diagram of the (a) H-cell and (b) flow-cell device.

electrosynthesis remains at an early stage. (1) Key challenges include gas diffusion layer flooding due to electrolyte penetration, which disrupts the stable three-phase interface and impedes CO_2 transport. (2) Catalyst detachment or degradation under high current density operation, which compromises long-term stability. (3) Carbonate precipitation in alkaline conditions, which can block pores and deactivate active sites. Addressing these issues requires advances in electrode architecture design, hydrophobic layer optimization, and the development of durable catalyst-substrate interfaces. The key aspects requiring further development include: optimization of catalyst loading and distribution; design of microporous layers to improve gas–liquid management; regulation of reaction flow rate; selection of ion exchange membranes to inhibit cross-reactions and improve stability; and overall reactor architecture to achieve scalability and long-term operation. Solving these challenges is crucial for advancing this technology to practical large-scale applications.

5 Conclusion and outlook

The electrocatalytic synthesis of urea using CO_2 and NO_3^- represents a highly promising green alternative, capable of effectively replacing the energy-intensive traditional Bosch–Meiser process [128]. This review systematically explores the key challenges in C–N coupling: the slow kinetics of the C–N coupling reaction and the mismatch between the reactant concentrations of CO_2RR and NO_3RR. Mechanism insights derived from *in-situ* spectroscopy and DFT calculations further clarify possible C–N coupling pathways, such as *CO-NH_2, *CO-NO, and *CO_2-NO_2 coupling, providing a basis for rational catalyst design. The advanced catalyst design and system engineering optimization strategies that have been published so far are analyzed to overcome these challenges [129–133]. These strategies address the imbalance in C–N coupling kinetics by promoting the synchronous activation and selective coupling of carbon and nitrogen intermediates, optimizing local reactant concentrations, and adjusting the reaction environment. Looking to the future, several key directions for application exploration must be pursued (Fig. 13):

(1) Spatial catalyst design: from zero-dimensional (0D) to three-dimensional (3D) spatial structures

Future catalysts can utilize the optimized reaction microenvironment designed from 0D to 3D spatial structures. At the nanoscale, precise control over pore and interlayer spacing (such as metal-organic framework materials, covalent organic framework materials, and layered materials) enables the enrichment and arrangement of key intermediates. From the 3D spatial structure, HoMS [104, 134–138] have ordered cavities and shells, forming partitioned areas, thereby facilitating the local aggregation of reactants, prolonging the interaction time of intermediates, and enhancing the probability of C–N coupling. Such design principles can be further extended to one-dimensional (1D) channels, 2D interlayers, and 3D porous networks, establishing interconnected pathways for efficient material/electric charge transfer, while suppressing unnecessary side reactions.

(2) Advanced mechanistic understanding via *in-situ* characterization and computation

Although current *in-situ* characterization techniques and density functional theory simulations have identified possible C–N coupling pathways, the direct observation of transient intermediates (such as *CO, *NO, *CO_2NO_2) is still limited. Future work should combine time-resolved *in-situ* spectroscopy (such as ultrafast infrared, Raman, and X-ray absorption) with machine learning-enhanced molecular dynamics to dynamically track the evolution of reaction pathways and active sites.

(3) Optimization of electrolyte and reactor for scale-up

Most current studies still rely on H-cell in the laboratory. The transition to flow-cell is crucial for improving CO_2 transport efficiency and achieving high current density. The key challenges in device optimization include the uniformity of the catalyst layer, electrolyte leakage blocking channels, and long-term stability. Electrolyte optimization involves cation selection (such as K^+), anion selection, and pH control, which should be combined with reactor design to create a microenvironment conducive to urea formation. Additionally, for achieving large-scale production, it is necessary to be compatible with intermittent renewable energy power generation, enabling the system to operate dynamically.

(4) Standardization and techno-economic evaluation

This field urgently requires unified performance evaluation standards, covering catalyst loading, selectivity, and stability, to ensure comparability among different studies. At the same time, a

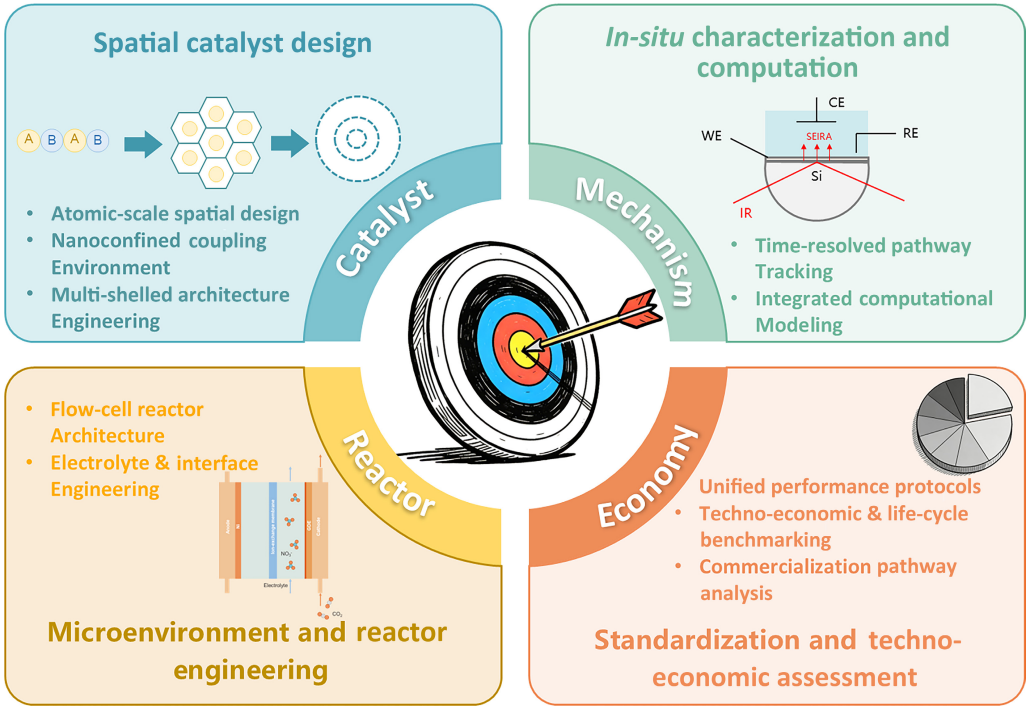

Figure 13 Roadmap for advancing electrocatalytic urea synthesis from CO_2 and NO_3^-.

rigorous techno-economic analysis and life cycle assessment should be conducted to compare electrocatalytic urea synthesis with traditional Haber–Bosch/Bosch–Mess routes and other green alternative solutions (such as urea production driven by green ammonia). Clearly defining the actual application scenarios, optimal operating conditions, and potential carbon/nitrogen footprints will help clarify the commercial feasibility and environmental benefits of this technology.

In summary, the synthesis of urea using CO_2 and NO_3^- through electrochemical methods is currently at an exciting intersection between basic science and emerging sustainable technologies. By integrating complex catalyst design, mechanistic analysis, device innovation, and comprehensive sustainability assessment, this field has the potential to make meaningful contributions to achieving carbon-neutral chemical production and global nitrogen management.

Data availability

All data needed to support the conclusions in the paper are presented in the manuscript. Additional data related to this paper may be requested from the corresponding author upon request.

Acknowledgements

This work was supported by the National Key Research and Development Program of China (No. 2024YFA1509400), the National Natural Science Foundation of China (Nos. 22293043, 92572205, 22505267, and 52272097), Shenzhen University 2035 Program for Excellent Research (No. 2024B005), Beijing Natural Science Foundation (No. 2242019), and IPE Project for Frontier Basic Research, China (No. QYJC-2023-08). Dan Wang thanks the Financial Support for Outstanding scientific and technological innovation Talents Training Fund in Shenzhen.

Declaration of competing interest

The authors declare no competing financial interest.

Author contribution statement

Q. X.： Original draft, writing – review & editing. C. C.: Writing – review & editing. D. L., J. Y. Z., and Y. N. C.: Review & editing. J. W. W., R. B. Y., and D. W.: Conceptualization, methodology, project administration, resources, writing – review & editing. All the authors have approved the final manuscript.

Use of AI statement

None.

References

[1] Chen, C.; Zhu, X. R.; Wen, X. J.; Zhou, Y. Y.; Zhou, L.; Li, H.; Tao, L.; Li, Q. L.; Du, S. Q.; Liu, T. T. et al. Coupling N_2 and CO_2 in H_2O to synthesize urea under ambient conditions. *Nat. Chem.* **2020**, *12*, 717–724.

[2] Zhu, X. R.; Zhou, X. C.; Jing, Y.; Li, Y. F. Electrochemical synthesis of urea on MBenes. *Nat. Commun.* **2021**, *12*, 4080.

[3] Yu, Y. D.; Lv, Z.; Liu, Z. Y.; Sun, Y. Y.; Wei, Y. Y.; Ji, X.; Li, Y. Y.; Li, H. D.; Wang, L.; Lai, J. P. Activation of Ga liquid catalyst with continuously exposed active sites for electrocatalytic C–N coupling. *Angew. Chem., Int. Ed.* **2024**, *63*, e202402236.

[4] Kyriakou, V.; Garagounis, I.; Vourros, A.; Vasileiou, E.; Stoukides, M. An electrochemical haber-bosch process. *Joule* **2020**, *4*, 142–158.

[5] IEA. *Ammonia Technology Roadmap*; IEA: Paris, 2021.

[6] Zhang, X. R.; Zhu, X. R.; Bo, S. W.; Chen, C.; Cheng, K.; Zheng, J. Y.; Li, S.; Tu, X. J.; Chen, W.; Xie, C. et al. Electrocatalytic urea synthesis with 63.5% Faradaic efficiency and 100% N-selectivity via one-step C–N coupling. *Angew. Chem., Int. Ed.* **2023**, *62*, e202305447.

[7] Shi, C. W.; Xia, K.; Zhang, L. L.; Guo, M. X.; Guan, X. P.; Gu, C. L.; Yang, X. L.; Wang, Y.; Liu, X.; Ding, X. Nitric acid-mediated

artificial urea photo-synthesis with N_2 and CO_2. *Adv. Energy Mater.* **2024**, *14*, 2400201.

[8] Peng, X. Y.; Zeng, L. B.; Wang, D. S.; Liu, Z. B.; Li, Y.; Li, Z. J.; Yang, B.; Lei, L. C.; Dai, L. M.; Hou, Y. Electrochemical C–N coupling of CO_2 and nitrogenous small molecules for the electrosynthesis of organonitrogen compounds. *Chem. Soc. Rev.* **2023**, *52*, 2193–2237.

[9] Chen, D. W.; Liu, J. N.; Shen, J. J.; Zhang, Y. Q.; Shao, H. Y.; Chen, C.; Wang, S. Y. Electrocatalytic C–N couplings at cathode and anode. *Adv. Energy Mater.* **2024**, *14*, 2303820.

[10] Bo, Y. N.; Wang, H. Y.; Lin, Y. X.; Yang, T.; Ye, R.; Li, Y.; Hu, C. Y.; Du, P. Y.; Hu, Y. G.; Liu, Z. et al. Altering hydrogenation pathways in photocatalytic nitrogen fixation by tuning local electronic structure of oxygen vacancy with dopant. *Angew. Chem., Int. Ed.* **2021**, *60*, 16085–16092.

[11] Xue, X. L.; Chen, R. P.; Yan, C. Z.; Zhao, P. Y.; Hu, Y.; Zhang, W. J.; Yang, S. Y.; Jin, Z. Review on photocatalytic and electrocatalytic artificial nitrogen fixation for ammonia synthesis at mild conditions: Advances, challenges and perspectives. *Nano Res.* **2019**, *12*, 1229–1249.

[12] Liu, J. X.; Smith, S. C.; Gu, Y. T.; Kou, L. Z. C–N coupling enabled by N–N bond breaking for electrochemical urea production. *Adv. Funct. Mater.* **2023**, *33*, 2305894.

[13] Kohlhaas, Y.; Tschauder, Y. S.; Plischka, W.; Simon, U.; Eichel, R. A.; Wessling, M.; Keller, R. Electrochemical urea synthesis. *Joule* **2024**, *8*, 1579–1600.

[14] Li, D.; Yang, K. X.; Lian, J. H.; Yan, J. Q.; Liu, S. Z. Powering the world with solar fuels from photoelectrochemical CO_2 reduction: Basic principles and recent advances. *Adv. Energy Mater.* **2022**, *12*, 2201070.

[15] Jin, S.; Hao, Z. M.; Zhang, K.; Yan, Z. H.; Chen, J. Advances and challenges for the electrochemical reduction of CO_2 to CO: From fundamentals to industrialization. *Angew. Chem., Int. Ed.* **2021**, *60*, 20627–20648.

[16] Li, J. N.; Zhang, Y. X.; Kuruvinashetti, K.; Kornienko, N. Construction of C–N bonds from small-molecule precursors through heterogeneous electrocatalysis. *Nat. Rev. Chem.* **2022**, *6*, 303–319.

[17] Jiao, Y. R.; Li, H. B.; Jiao, Y.; Qiao, S. Z. Activity and selectivity roadmap for C–N electro-coupling on MXenes. *J. Am. Chem. Soc.* **2023**, *145*, 15572–15580.

[18] Gerke, C. S.; Xu, Y. T.; Yang, Y. W.; Foley, G. D.; Zhang, B.; Shi, E.; Bedford, N. M.; Che, F. L.; Thoi, V. S. Electrochemical C–N bond formation within boron imidazolate cages featuring single copper sites. *J. Am. Chem. Soc.* **2023**, *145*, 26144–26151.

[19] Zhang, J. J.; Zhang, Y. F.; Qin, Z. X.; Li, Z. W.; Tong, Z. H.; Zhao, Z.; Gascón, J. A.; Li, G. How carbene ligands transform AuAg Alloy nanoclusters for electrocatalytic urea synthesis. *Angew. Chem., Int. Ed.* **2025**, *64*, e202420993.

[20] Lu, X. M.; Song, H. Q.; Cai, J. M.; Lu, S. Y. Recent development of electrochemical nitrate reduction to ammonia: A mini review. *Electrochem. Commun.* **2021**, *129*, 107094.

[21] Bui, J. C.; Lees, E. W.; Pant, L. M.; Zenyuk, I. V.; Bell, A. T.; Weber, A. Z. Continuum modeling of porous electrodes for electrochemical synthesis. *Chem. Rev.* **2022**, *122*, 11022–11084.

[22] Cao, J. H.; Zhao, F.; Li, C. J.; Zhao, Q. D.; Gao, L. G.; Ma, T. L.; Xu, H.; Ren, X. F.; Liu, A. M. Electrocatalytic synthesis of urea: An in-depth investigation from material modification to mechanism analysis. *Small* **2024**, *20*, 2403412.

[23] Zhao, J. M.; Yuan, Y.; Kou, M. M.; Meng, F. P.; Lin, W.; Zhao, J. S.; Tsiakaras, P. Carbon dioxide and nitrate reduction reactions tailoring kinetics over Cu_2O with mesoporous carbon channels for boosting electrocatalytic urea synthesis. *J. Environ. Chem. Eng.* **2024**, *12*, 114959.

[24] Tao, Z. X.; Rooney, C. L.; Liang, Y. Y.; Wang, H. L. Accessing organonitrogen compounds via C–N coupling in electrocatalytic CO_2 reduction. *J. Am. Chem. Soc.* **2021**, *143*, 19630–19642.

[25] Lv, C. D.; Zhong, L. X.; Liu, H. J.; Fang, Z. W.; Yan, C. S.; Chen, M. X.; Kong, Y.; Lee, C.; Liu, D. B.; Li, S. Z. et al. Selective electrocatalytic synthesis of urea with nitrate and carbon dioxide. *Nat. Sustain.* **2021**, *4*, 868–876.

[26] Jiang, M. H.; Zhu, M. F.; Wang, M. J.; He, Y.; Luo, X. J.; Wu, C. J.; Zhang, L. Y.; Jin, Z. Review on electrocatalytic coreduction of carbon dioxide and nitrogenous species for urea synthesis. *ACS Nano* **2023**, *17*, 3209–3224.

[27] Zhao, Y. L.; Ding, Y. X.; Li, W. L.; Liu, C.; Li, Y. Z.; Zhao, Z. Q.; Shan, Y.; Li, F.; Sun, L. C.; Li, F. S. Efficient urea electrosynthesis from carbon dioxide and nitrate via alternating Cu-W bimetallic C–N coupling sites. *Nat. Commun.* **2023**, *14*, 4491.

[28] Meng, N. N.; Huang, Y. M.; Liu, Y.; Yu, Y. F.; Zhang, B. Electrosynthesis of urea from nitrite and CO_2 over oxygen vacancy-rich ZnO porous nanosheets. *Cell Rep. Phys. Sci.* **2021**, *2*, 100378.

[29] Wang, Z. C.; Wang, M. F.; Cheng, Q. Y.; He, Y. Z.; Jiang, Y. Z.; Liu, S. S.; Qian, T.; Xiong, J.; Yang, C. T.; Yan, C. L. Polycation-functionalized interface enable *in situ* capturing of CO_2 and filtering of proton for efficient C–N coupling toward highly selective urea electrosynthesis. *Chem. Eng. J.* **2024**, *492*, 152161.

[30] Shi, R.; Guo, J. H.; Zhang, X. R.; Waterhouse, G. I. N.; Han, Z. J.; Zhao, Y. X.; Shang, L.; Zhou, C.; Jiang, L.; Zhang, T. R. Efficient wettability-controlled electroreduction of CO_2 to CO at Au/C interfaces. *Nat. Commun.* **2020**, *11*, 3028.

[31] Zhang, H. J.; Fang, K. Q.; Yang, J.; Chen, H.; Ning, J. Q.; Wang, H. Y.; Hu, Y. Strategies and applications of electrocatalytic nitrate reduction towards ammonia. *Coord. Chem. Rev.* **2024**, *506*, 215723.

[32] Zhou, Y. F.; Xing, G. S.; Sun, C. H.; Chen, Z. K.; Li, S. Y.; Yang, R.; Chen, M.; Zhang, P.; Feng, C. R.; Abudula, A. et al. Electrosynthesis of urea from carbon dioxide and waste nitrates: History, recent progress, and future prospects. *Adv. Funct. Mater.* **2026**, *36*, e15635.

[33] Cai, J.; Wang, Z. X.; Zheng, X.; Hao, J. C.; Bao, K. L.; Zhou, Y.; Pan, X. D.; Zhu, H. Advances in electrocatalytic urea synthesis: Detection methods, C–N coupling mechanisms, and catalyst design. *Nano Res.* **2025**, *18*, 94907232.

[34] Wan, Y. C.; Zheng, M. Y.; Yan, W.; Zhang, J. J.; Lv, R. T. Fundamentals and rational design of heterogeneous C–N coupling electrocatalysts for urea synthesis at ambient conditions. *Adv. Energy Mater.* **2024**, *14*, 2303588.

[35] Wu, Q.; Dai, C. C.; Meng, F. X.; Jiao, Y.; Xu, Z. J. Potential and electric double-layer effect in electrocatalytic urea synthesis. *Nat. Commun.* **2024**, *15*, 1095.

[36] Liu, X.; Jiao, Y.; Zheng, Y.; Jaroniec, M.; Qiao, S. Z. Mechanism of C–N bonds formation in electrocatalytic urea production revealed by *ab initio* molecular dynamics simulation. *Nat. Commun.* **2022**, *13*, 5471.

[37] Zhao, Q. L.; Lu, X. X.; Wang, Y. N.; Zhu, S. Q.; Liu, Y. S.; Xiao, F.; Dou, S. X.; Lai, W. H.; Shao, M. H. Sustainable and high-rate electrosynthesis of nitrogen fertilizer. *Angew. Chem., Int. Ed.* **2023**, *62*, e202307123.

[38] Liu, J. X.; Guo, X. Y.; Frauenheim, T.; Gu, Y. T.; Kou, L. Z. Urea electrosynthesis accelerated by theoretical simulations. *Adv. Funct. Mater.* **2024**, *34*, 2313420.

[39] Shibata, M.; Furuya, N. Electrochemical synthesis of urea at gas-diffusion electrodes: Part VI. Simultaneous reduction of carbon dioxide and nitrite ions with various metallophthalocyanine catalysts. *J. Electroanal. Chem.* **2001**, *507*, 177–184.

[40] Shibata, M.; Yoshida, K.; Furuya, N. Electrochemical synthesis of urea on reduction of carbon dioxide with nitrate and nitrite ions using Cu-loaded gas-diffusion electrode. *J. Electroanal. Chem.* **1995**, *387*, 143–145.

[41] Feng, Y. G.; Yang, H.; Zhang, Y.; Huang, X. Q.; Li, L. G.; Cheng, T.; Shao, Q. Te-doped Pd nanocrystal for electrochemical urea production by efficiently coupling carbon dioxide reduction with nitrite reduction. *Nano Lett.* **2020**, *20*, 8282–8289.

[42] Wang, Y.; Xia, S.; Zhang, J. F.; Li, Z. Y.; Cai, R.; Yu, C. P.; Zhang, Y.; Wu, J. J.; Wu, Y. C. Spatial management of CO diffusion on

tandem electrode promotes NH_2 intermediate formation for efficient urea electrosynthesis. *ACS Energy Lett.* **2023**, *8*, 3373–3380.

[43] Sun, Z. Y.; Niu, R.; Shang, S. Y.; Guo, Y. L.; Zhang, H.; Liu, X. J.; Feng, L. B.; Chu, K. Plasma-electrocatalytic synthesis of urea from air and CO_2. *Nat. Commun.* **2025**, *16*, 8837.

[44] Leverett, J.; Tran-Phu, T.; Yuwono, J. A.; Kumar, P.; Kim, C.; Zhai, Q. F.; Han, C.; Qu, J. T.; Cairney, J.; Simonov, A. N. et al. Tuning the coordination structure of Cu-N-C single atom catalysts for simultaneous electrochemical reduction of CO_2 and NO_3^- to urea. *Adv. Energy Mater.* **2022**, *12*, 2201500.

[45] Wei, X. X.; Wen, X. J.; Liu, Y. Y.; Chen, C.; Xie, C.; Wang, D. D.; Qiu, M. Y.; He, N. H.; Zhou, P.; Chen, W. et al. Oxygen vacancy-mediated selective C–N coupling toward electrocatalytic urea synthesis. *J. Am. Chem. Soc.* **2022**, *144*, 11530–11535.

[46] Tu, X. J.; Zhu, X. R.; Bo, S. W.; Zhang, X. R.; Miao, R. P.; Wen, G. B.; Chen, C.; Li, J.; Zhou, Y. Y.; Liu, Q. H. et al. A universal approach for sustainable urea synthesis via intermediate assembly at the electrode/electrolyte interface. *Angew. Chem., Int. Ed.* **2024**, *63*, e202317087.

[47] Chen, M. Y.; Zhu, X. R.; Qin, X. P.; Guo, N. N.; Wang, L. X.; Sun, H. X.; Liu, Q. H.; Chen, C.; Wang, S. Y. Molecule engineering on copper-based electrocatalyst toward electrocatalytic C–N coupling for urea synthesis. *Adv. Funct. Mater.* **2026**, *36*, e16741.

[48] Du, W. Y.; Sun, Z. Y.; Chen, K.; Wei, Y. C.; Bao, R.; Chu, K. Synergistic Cu single atoms and MoS_2-edges for tandem electrocatalytic reduction of NO_3^- and CO_2 to urea. *Adv. Energy Mater.* **2024**, *14*, 2401765.

[49] Chen, K.; Ma, D. Y.; Zhang, Y.; Wang, F. Z.; Yang, X.; Wang, X. M.; Zhang, H.; Liu, X. J.; Bao, R.; Chu, K. Urea electrosynthesis from nitrate and CO_2 on diatomic alloys. *Adv. Mater.* **2024**, *36*, 2402160.

[50] Hu, B. H.; Lu, R. H.; Wang, W. L.; Zhou, Y. F.; Jaswanthi, D. K. D.; Wu, Z.; Wang, Z. Y.; Wang, L. Directing the C–N coupling pathway enables efficient urea electrosynthesis. *J. Am. Chem. Soc.* **2025**, *147*, 21764–21777.

[51] Chen, X. K.; Tan, Y.; Yuan, J.; Zhai, S. L.; Su, L.; Mou, Y. J.; Deng, W. Q.; Wu, H. Enhancing urea electrosynthesis from CO_2 and nitrate through high-entropy alloying. *Adv. Energy Mater.* **2025**, *15*, 2500872.

[52] Luo, Y. T.; Xie, K.; Ou, P. F.; Lavallais, C.; Peng, T.; Chen, Z.; Zhang, Z. Y.; Wang, N.; Li, X. Y.; Grigioni, I. et al. Selective electrochemical synthesis of urea from nitrate and CO_2 via relay catalysis on hybrid catalysts. *Nat. Catal.* **2023**, *6*, 939–948.

[53] Wang, Y. J.; Zhu, X. R.; An, Q. Z.; Zhang, X. R.; Wei, X. X.; Chen, C.; Li, H.; Chen, D. W.; Zhou, Y. Y.; Liu, Q. H. et al. Electron deficiency is more important than conductivity in C–N coupling for electrocatalytic urea synthesis. *Angew. Chem., Int. Ed.* **2024**, *63*, e202410938.

[54] Liang, J. Y.; Deng, S. J.; Li, Z. Y.; Zhou, M.; Wang, S.; Su, Y. Q.; Yang, S.; Li, H. Spin state modulation with oxygen vacancy orientates C/N intermediates for urea electrosynthesis of ultrahigh efficiency. *Adv. Mater.* **2025**, *37*, 2418828.

[55] Gong, C. T.; Peng, Y. W.; Xu, M. Q.; Wei, X. F.; Sheng, G.; Liu, J. L.; Wu, X. W.; Han, X.; Dai, F. N.; Dong, J. Q. et al. Selective electrocatalytic synthesis of urea using entangled iron porphyrins in covalent organic frameworks. *Nat. Synth.* **2025**, *4*, 720–729.

[56] Li, J. Y.; Li, Y. F.; Li, L. S.; Jiang, Z.; Chen, Y.; Xia, B. Y. Remote carbon monoxide spillover improves tandem urea electrosynthesis. *Angew. Chem., Int. Ed.* **2025**, *64*, e202421266.

[57] Hu, Q.; Zhou, W. L.; Qi, S.; Huo, Q. H.; Li, X.; Lv, M. Y.; Chen, X. B.; Feng, C.; Yu, J. Y.; Chai, X. Y. et al. Pulsed co-electrolysis of carbon dioxide and nitrate for sustainable urea synthesis. *Nat. Sustain.* **2024**, *7*, 442–451.

[58] Liu, X. F.; Feng, J.; Cheng, X. F.; Zhang, J. C.; Huo, J. Y.; Chen, D. Y.; Marcomini, A.; Li, Y. Y.; Xu, Q. F.; Lu, J. M. High C-selectivity for urea synthesis through O-philic adsorption to form *OCO intermediate on Ti-MOF based electrocatalysts. *Adv. Funct. Mater.* **2024**, *34*, 2400892.

[59] Zhang, X.; Sun, H.; Wang, Y. R.; Shi, Z.; Zhong, R. L.; Sun, C. Y.; Liu, J. Y.; Su, Z. M.; Lan, Y. Q. Dynamic control of asymmetric charge distribution for electrocatalytic urea synthesis. *Adv. Mater.* **2024**, *36*, 2408510.

[60] Huang, X. M.; Li, Y. F.; Xie, S. J.; Zhao, Q.; Zhang, B. Y.; Zhang, Z. Y.; Sheng, H.; Zhao, J. C. The tandem nitrate and CO_2 reduction for urea electrosynthesis: Role of surface N-intermediates in CO_2 capture and activation. *Angew. Chem., Int. Ed.* **2024**, *63*, e202403980.

[61] Wei, X. X.; Liu, Y. Y.; Zhu, X. R.; Bo, S. W.; Xiao, L.; Chen, C.; Nga, T. T. T.; He, Y. Q.; Qiu, M. Y.; Xie, C. et al. Dynamic reconstitution between copper single atoms and clusters for electrocatalytic urea synthesis. *Adv. Mater.* **2023**, *35*, 2300020.

[62] Yang, Y. D.; Wu, G. Z.; Jiang, J. D.; Zhang, W. Y.; Liu, S. J.; Yu, R.; Liu, F. K.; Du, A. J.; Dai, L.; Mao, X. et al. Stabilization of $Cu^{\delta+}$ sites within MnO_2 for superior urea electro-synthesis. *Adv. Mater.* **2024**, *36*, 2409697.

[63] Gao, Y. H.; Wang, J. N.; Sun, M. L.; Jing, Y.; Chen, L. L.; Liang, Z. Q.; Yang, Y. J.; Zhang, C.; Yao, J. N.; Wang, X. Tandem catalysts enabling efficient C–N coupling toward the electrosynthesis of urea. *Angew. Chem., Int. Ed.* **2024**, *63*, e202402215.

[64] Huang, D. S.; Qiu, X. F.; Huang, J. R.; Mao, M.; Liu, L. M.; Han, Y.; Zhao, Z. H.; Liao, P. Q.; Chen, X. M. Electrosynthesis of urea by using Fe_2O_3 nanoparticles encapsulated in a conductive metal-organic framework. *Nat. Synth.* **2024**, *3*, 1404–1413.

[65] Chen, X. Y.; Lv, S. N.; Gu, H. F.; Cui, H. K.; Liu, G.; Liu, Y. F.; Li, Z. Y.; Xu, Z. Y.; Kang, J. X.; Teobaldi, G. et al. Amorphous bismuth-tin oxide nanosheets with optimized C–N coupling for efficient urea synthesis. *J. Am. Chem. Soc.* **2024**, *146*, 13527–13535.

[66] Zhang, X. R.; Zhu, X. R.; Bo, S. W.; Chen, C.; Qiu, M. Y.; Wei, X. X.; He, N. H.; Xie, C.; Chen, W.; Zheng, J. Y. et al. Identifying and tailoring C–N coupling site for efficient urea synthesis over diatomic Fe–Ni catalyst. *Nat. Commun.* **2022**, *13*, 5337.

[67] Qiu, M. Y.; Zhu, X. R.; Bo, S. W.; Cheng, K.; He, N. H.; Gu, K. Z.; Song, D. Z.; Chen, C.; Wei, X. X.; Wang, D. D. et al. Boosting electrocatalytic urea production via promoting asymmetric C–N coupling. *CCS Chem.* **2023**, *5*, 2617–2627.

[68] Cheng, M. Y.; Wang, S.; Dai, Z. C.; Xia, J.; Zhang, B. C.; Feng, P. Y.; Zhu, Y.; Zhang, Y. Y.; Zhang, G. Q. Rectifying heterointerface facilitated C–N coupling dynamics enables efficient urea electrosynthesis under ultralow potentials. *Angew. Chem., Int. Ed.* **2025**, *64*, e202413534.

[69] Geng, J.; Ji, S. H.; Jin, M.; Zhang, C.; Xu, M.; Wang, G. Z.; Liang, C. H.; Zhang, H. M. Ambient electrosynthesis of urea with nitrate and carbon dioxide over iron-based dual-sites. *Angew. Chem., Int. Ed.* **2023**, *62*, e202210958.

[70] Zhang, Y.; Li, Z. H.; Chen, K.; Yang, X.; Zhang, H.; Liu, X. J.; Chu, K. Promoting electroreduction of CO_2 and NO_3^- to urea via tandem catalysis of zn single atoms and In_2O_{3-x}. *Adv. Energy Mater.* **2024**, *14*, 2402309.

[71] Zhao, C.; Jin, Y.; Yuan, J. K.; Hou, Q. L.; Li, H.; Yan, X. Q.; Ou, H. H.; Yang, G. D. Tailoring activation intermediates of CO_2 initiates C–N coupling for highly selective urea electrosynthesis. *J. Am. Chem. Soc.* **2025**, *147*, 8871–8880.

[72] Liu, J. F.; Zhang, S. B.; Mao, Z. X.; Li, W. Y.; Jin, M.; Yin, H. J.; Zhang, Y. X.; Wang, G. Z.; Zhang, H. M.; Zhao, H. J. *In-situ* electrochemical reconstruction of copper single-sites to dual-sites for ambient urea synthesis. *Angew. Chem., Int. Ed.* **2025**, *64*, e202509385.

[73] Zhang, K. F.; Liu, Y. Y.; Qin, X. P.; Hou, P. L.; Zhang, C.; Yan, D. F.; Lv, C. D.; Chen, D. W.; Feng, Y.; Wu, Z. et al. Designing molecular reactor of interlayer dual-atom toward urea electrosynthesis. *Angew. Chem., Int. Ed.* **2025**, *64*, e202513341.

[74] Zhao, J. M.; Yuan, Y.; Zhao, F.; Han, W.; Yuan, Q.; Kou, M. M.; Zhao, J. S.; Chen, C.; Wang, S. Y. Identifying the facet-dependent active sites of Cu_2O for selective C–N coupling toward

electrocatalytic urea synthesis. *Appl. Catal. B: Environ.* **2024**, *340*, 123265.

[75] Li, H.; Xu, L. T.; Bo, S. W.; Wang, Y. J.; Xu, H.; Chen, C.; Miao, R. P.; Chen, D. W.; Zhang, K. F.; Liu, Q. H. et al. Ligand engineering towards electrocatalytic urea synthesis on a molecular catalyst. *Nat. Commun.* **2024**, *15*, 8858.

[76] Yu, X.; Zeng, S. Q.; Li, L.; Yao, H.; Zheng, Y. N.; Guo, X. H. Synergistic coupling of CO_2 and NO_3-for efficient electrosynthesis of urea using oxygen vacancy-rich Ru-doped CeO_2 nanorods. *Sci. China Mater.* **2024**, *67*, 1543–1550.

[77] Mao, Y. N.; Jiang, Y.; Gou, Q.; Lv, S. M.; Song, Z. Y.; Jiang, Y. M.; Wang, W. B.; Li, M.; Zheng, L. R.; Su, W. et al. Indium-activated bismuth-based catalysts for efficient electrocatalytic synthesis of urea. *Appl. Catal. B: Environ.* **2024**, *340*, 123189.

[78] Wu, Y. J.; Lin, H.; Mao, Q. Q.; Yu, H. J.; Deng, K.; Wang, J. G.; Wang, L.; Wang, Z. Q.; Wang, H. J. Trace Cu-induced low C–N coupling barrier on amorphous co metallene boride for boosting electrochemical urea production. *Small* **2024**, *20*, 2407679.

[79] Miao, R. P.; Qin, X. P.; Wang, Y. J.; Wang, S. Q.; Gu, K. Z.; Zhou, Y. Y.; Chen, D. W.; Yan, D. F.; Gao, W. Q.; Liu, Q. H. et al. Closing electron transfer loop to boost electrocatalytic urea synthesis. *Angew. Chem., Int. Ed.* **2025**, *64*, e202517450.

[80] Kou, M. M.; Yuan, Y.; Ma, J. M.; Shao, R. H.; Zhao, J. M.; Yuan, Q.; Zhao, J. S. Single-atom cu sites with engineered oxygen vacancies boost electrocatalytic urea production from CO_2 and nitrate. *J. Colloid Interface Sci.* **2026**, *704*, 139350.

[81] Liu, C. C.; Tong, H. L.; Wang, P. F.; Huang, R.; Huang, P. L.; Zhou, G.; Liu, L. Z. The asymmetric orbital hybridization in single-atom-dimers for urea synthesis by optimizing the C–N coupling reaction pathway. *Appl. Catal. B: Environ.* **2023**, *336*, 122917.

[82] Lv, C. D.; Lee, C.; Zhong, L. X.; Liu, H. J.; Liu, J. W.; Yang, L.; Yan, C. S.; Yu, W.; Hng, H. H.; Qi, Z. M. et al. A defect engineered electrocatalyst that promotes high-efficiency urea synthesis under ambient conditions. *ACS Nano* **2022**, *16*, 8213–8222.

[83] Tan, Y.; Chen, X. K.; Yuan, J.; Sheng, G.; Deng, W. Q.; Wu, H. Concentration-adaptive electrocatalytic urea synthesis from CO_2 and nitrate via porphyrin and metalloporphyrin MOFs. *Angew. Chem., Int. Ed.* **2025**, *64*, e202513441.

[84] Cheng, Z.; Wang, X. D.; Yan, D. F.; Qin, X. P.; Chen, D. W.; Zhang, C.; Wang, Y. J.; Zhou, Y. S.; Lv, C. D.; Hou, P. L. et al. Achieving record-breaking urea synthesis on crystalline-amorphous hybrid via electrochemical-chemical looping. *J. Am. Chem. Soc.* **2025**, *147*, 39761–39769.

[85] Qiu, W. B.; Qin, S. M.; Li, Y. B.; Cao, N.; Cui, W. R.; Zhang, Z. D.; Zhuang, Z. C.; Wang, D. S.; Zhang, Y. Overcoming electrostatic interaction via pulsed electroreduction for boosting the electrocatalytic urea synthesis. *Angew. Chem., Int. Ed.* **2024**, *63*, e202402684.

[86] Niu, R.; Sun, Z. Y.; Qian, J. M.; Guo, Y. L.; Ma, D. W.; Chu, K. Efficient urea electrosynthesis via the synergy of self-tandem catalysis and HMF oxidation. *Chem. Eng. J.* **2025**, *525*, 169931.

[87] Mao, Y. N.; Jiang, Y.; Liu, H.; Jiang, Y. M.; Li, M.; Su, W.; He, R. X. Ambient electrocatalytic synthesis of urea by co-reduction of NO_3^- and CO_2 over graphene-supported In_2O_3. *Chin. Chem. Lett.* **2024**, *35*, 108540.

[88] Sun, Z. S.; Xiang, X. Y.; Zhao, Q. P.; Tang, Z.; Jiang, S. Y.; Lu, T. B.; Zhang, Z. M.; Wang, B. F.; Yin, H. Q. Efficient electrocatalytic urea synthesis from CO_2 and nitrate over the scale-up produced FeNi alloy-decorated nanoporous carbon. *Chin. J. Catal.* **2024**, *65*, 153–162.

[89] Yu, K. L.; Wang, H.; Yu, W. C.; Zhang, Z. B.; Bian, Z. Y. Selective coreduction of CO_2 and NO_3^- for urea synthesis via electrochemical pathway modulated by p-block metal-doped copper oxides. *Chem. Eng. J.* **2025**, *514*, 163048.

[90] Zhang, C.; Zhou, Q.; Li, Z. Y.; Yan, C. S.; Liu, H. J.; Liu, D. B.; Song, L.; Yan, Q. Y.; Lv, C. D. Promoting the intermediates hydrogenation for urea electrosynthesis over an "active hydrogen pump" catalyst. *Angew. Chem., Int. Ed.* **2025**, *64*, e202507869.

[91] Liu, X. W.; Kumar, P. V.; Chen, Q.; Zhao, L. J.; Ye, F. H.; Ma, X. Y.; Liu, D.; Chen, X. C.; Dai, L. M.; Hu, C. G. Carbon nanotubes with fluorine-rich surface as metal-free electrocatalyst for effective synthesis of urea from nitrate and CO_2. *Appl. Catal. B: Environ.* **2022**, *316*, 121618.

[92] Wu, Q. L.; Wu, L. Y.; Han, Y.; Zou, H. Y.; Su, X. Z.; Chu, Y. H.; Deng, H.; Tang, S. R.; Wang, X. K.; Zhang, D. D. et al. Spatially matched C–N coupling within carbon defect confined interlayer Fe clusters for efficient urea electrosynthesis. *Adv. Mater.* **2026**, *38*, e14503.

[93] Chen, L. Y.; Yang, S.; Yao, S. Y.; Si, Z. H.; Ding, G. C.; Zhan, P.; Song, J.; Cui, M.; Lu, L.; Qin, P. Y. Modulating adsorption configuration of intermediates on Cu–In dual-atom catalyst for boosted urea electrosynthesis. *App. Catal. B: Environ.* **2025**, *379*, 125710.

[94] Qian, Q. Z.; Liu, Q. L.; Wang, M. X.; Yang, J. J.; Li, H. Y.; Bai, W.; Wang, W. T.; Wu, C. Z.; Xiao, C.; Xie, Y. Dual-site cooperation for synergistic optimization of the band structure and spin state to facilitate C–N coupling reaction. *Proc. Natl. Acad. Sci. USA* **2025**, *122*, e2508077122.

[95] Yu, Y. C.; Ma, X. D.; Huang, Y. M.; Jiao, M. G.; Kong, L. J.; Zhang, B. Defect-induced triple synergistic modulation of CuBi clusters for enhanced urea electrosynthesis. *Angew. Chem., Int. Ed.* **2026**, *138*, e25147.

[96] Deng, T.; Jia, S. Q.; Xue, C.; Cheng, H. L.; Jiao, J. P.; Chen, X.; Xia, Z. H.; Dong, M. K.; Chen, C. J.; Wu, H. H. et al. Phosphorus-doped Cu/Fe_2O_3 electrocatalysts with optimized synergy between the different sites for efficient urea electrosynthesis. *J. Am. Chem. Soc.* **2025**, *147*, 32924–32931.

[97] Xu, M. Q.; Xue, Y. Y.; Liu, Z. Z.; Lv, X. M.; Han, Q.; Zheng, G. F. Efficient urea electrosynthesis on a Cu_3 molecular catalyst with dynamically adaptive intercopper spacings. *J. Am. Chem. Soc.* **2025**, *147*, 41956–41964.

[98] Xiao, Q.; Shang, L. L.; Peng, Y.; Zhang, L. D.; Wei, Y. Z.; Zhao, D. C.; Zhao, Y. S.; Wan, J. W.; Wang, Y. G.; Wang, D. Rational design of coordination polymers composited hollow multishelled structures for drug delivery. *Small Methods* **2025**, *9*, 2301664.

[99] Wang, J. Y.; Tang, H. J.; Zhang, L. J.; Ren, H.; Yu, R. B.; Jin, Q.; Qi, J.; Mao, D.; Yang, M.; Wang, Y. et al. Multi-shelled metal oxides prepared via an anion-adsorption mechanism for lithium-ion batteries. *Nat. Energy* **2016**, *1*, 16050.

[100] Rao, F.; Xiao, Q.; Wei, Y. Z.; Wang, J. Y.; Yu, R. B.; Wang, D. Balanced polysulfide containment and lithium ion transport in lithium-sulfur batteries via nitrogen-doped carbon hollow multi-shelled structures on modified separators. *Chem. Res. Chin. Univ.* **2024**, *40*, 690–698.

[101] Wang, J. Y.; Wan, J. W.; Yang, N. L.; Li, Q.; Wang, D. Hollow multishell structures exercise temporal-spatial ordering and dynamic smart behaviour. *Nat. Rev. Chem.* **2020**, *4*, 159–168.

[102] Wei, Y. Z.; Li, J.; Zhao, D. C.; Zhao, Y. S.; Zhang, Q. H.; Gu, L.; Wan, J. W.; Wang, D. ZnO HoMS@ZIF-8 nanoreactors for efficient enrichment and photoreduction of atmospheric CO_2. *CCS Chem.* **2024**, *6*, 3065–3076.

[103] Du, J. X.; Wu, Y. S.; Fang, S. Y.; Xu, D. L.; Liu, M.; Liang, H.; Wu, Z. B.; Lu, G. M.; Wu, X. H. Nano-confinement engineering boosts C–N coupling for urea electrosynthesis. *Nat. Commun.* **2026**, *17*, 1008.

[104] Wei, Y. Z.; Zhao, D. C.; Wang, D. Mesoscience in hollow multi-shelled structures. *Adv. Sci.* **2024**, *11*, 2305408.

[105] Fan, X.; Li, D. H.; Shu, Y. X.; Feng, Y. M.; Li, F. X. Confinement effect and application in catalytic oxidation-reduction reaction of confined single-atom catalysts. *ACS Catal.* **2024**, *14*, 12991–13014.

[106] Zhang, J.; Tian, Y. F.; Xin, S.; Guo, Y. G. Space-confined electrochemical reactions and materials for high-energy-density batteries. *Acc. Mater. Res.* **2023**, *4*, 580–590.

[107] Dutta, N.; Giri, B.; Riyaz, M.; Midya, S.; Singh, A.; Bagchi, D.;

Mondal, S.; Kediya, S.; Singh, A. K.; Chakraborty, S. et al. Confining reaction intermediates in oxide-derived hollow Cu-Zn bimetallic catalyst facilitates selective formation of C_{2+} alcohols from electrochemical carbon dioxide reduction. *Angew. Chem., Int. Ed.* **2026**, *138*, e23150.

[108] Han, L.; Li, Y.; Wang, X. Y.; Yao, Z. B.; Chen, Z. M.; Li, J. P.; Tan, T. W.; Lee, S. Y.; Lv, Y. Q. Spatially decoupled electro-biosystem for efficient CO_2-to-chemicals conversion via tandem catalysis. *Adv. Energy Mater.* **2025**, *15*, e03056.

[109] Li, N.; Gao, H.; Liu, Z. X.; Zhi, Q. J.; Li, B. W.; Gong, L.; Chen, B. T.; Yang, T.; Wang, K.; Jin, P. et al. Metalphthalocyanine frameworks grown on TiO_2 nanotubes for synergistically and efficiently electrocatalyzing urea production from CO_2 and nitrate. *Sci. China Chem.* **2023**, *66*, 1417–1424.

[110] Wang, Z. C.; Wang, M. F.; Cheng, Q. Y.; He, Y. Z.; Liu, S. S.; Liu, J.; Yuan, X. L.; Huan, Y. F.; Qian, T.; Yan, C. L. Orderly coating of bilayer polymer to tailor microenvironment for efficient C–N coupling toward highly selective urea electrosynthesis. *Angew. Chem., Int. Ed.* **2025**, *64*, e202416832.

[111] Sun, H. M.; Yan, Z. H.; Liu, F. M.; Xu, W. C.; Cheng, F. Y.; Chen, J. Self-supported transition-metal-based electrocatalysts for hydrogen and oxygen evolution. *Adv. Mater.* **2020**, *32*, 1806326.

[112] Weekes, D. M.; Salvatore, D. A.; Reyes, A.; Huang, A. X.; Berlinguette, C. P. Electrolytic CO_2 reduction in a flow cell. *Acc. Chem. Res.* **2018**, *51*, 910–918.

[113] Huang, Y. M.; Yang, R.; Wang, C. H.; Meng, N. N.; Shi, Y. M.; Yu, Y. F.; Zhang, B. Direct electrosynthesis of urea from carbon dioxide and nitric oxide. *ACS Energy Lett.* **2022**, *7*, 284–291.

[114] Chi, L. P.; Zhang, Y. C.; Niu, Z. Z.; Zhang, X. L.; Li, Y. C.; Zhang, T. Y.; Sun, S. P.; Lu, P. G.; Tang, K. B.; Gao, M. R. Acidic CO_2 electrolysis with near-ideal selectivity and carbon efficiency enabled by overcoming its inherent trade-off. *Angew. Chem., Int. Ed.* **2025**, *64*, e202503539.

[115] Hicks, M. H.; Nie, W. X.; Boehme, A. E.; Atwater, H. A.; Agapie, T.; Peters, J. C. Electrochemical CO_2 reduction in acidic electrolytes: Spectroscopic evidence for local pH gradients. *J. Am. Chem. Soc.* **2024**, *146*, 25282–25289.

[116] Liu, J. W.; Fu, G. D.; Liao, Y. F.; Zhang, W. J.; Xi, X. A.; Si, F. Z.; Wang, L.; Zhang, J. J.; Fu, X. Z.; Luo, J. L. Electrochemical conversion of small organic molecules to value-added chemicals and hydrogen/electricity without CO_2 emission: Electrocatalysts, devices and mechanisms. *eScience* **2025**, *5*, 100267.

[117] Li, A.; Zhang, P.; Kan, E. J.; Gong, J. L. Wettability adjustment to enhance mass transfer for heterogeneous electrocatalysis and photocatalysis. *eScience* **2024**, *4*, 100157.

[118] Chen, F. R.; Yao, Z. C.; Lyu, Z. H.; Fu, J. J.; Zhang, X. L.; Hu, J. S. Recent advances in p-block metal chalcogenide electrocatalysts for high-efficiency CO_2 reduction. *eScience* **2024**, *4*, 100172.

[119] Xu, Z. C.; Wu, Z. S. Inner curved surface single Fe-atom catalysts for durable proton-exchange membrane fuel cells. *NSO* **2025**, *4*, 20250040.

[120] Gai, T. Y.; Ai, Y.; Li, W. Rare-earth-metal-alloyed mesoporous PtPb nanosheets for selective electrosynthesis of glyceric acid from glycerol upcycling. *NSO* **2025**, *4*, 20250042.

[121] Zhang, Z. M.; Wang, T.; Cai, Y. C.; Li, X. Y.; Ye, J. Y.; Zhou, Y.; Tian, N.; Zhou, Z. Y.; Sun, S. G. Probing electrolyte effects on cation-enhanced CO_2 reduction on copper in acidic media. *Nat. Catal.* **2024**, *7*, 807–817.

[122] Xu, Y. F.; Xia, Z. M.; Gao, W. Q.; Xiao, H.; Xu, B. J. Cation effect on the elementary steps of the electrochemical CO reduction reaction on Cu. *Nat. Catal.* **2024**, *7*, 1120–1129.

[123] Fan, M. Y.; Huang, J. E.; Miao, R. K.; Mao, Y.; Ou, P. F.; Li, F.; Li, X. Y.; Cao, Y. F.; Zhang, Z. S.; Zhang, J. Q. et al. Cationic-group-functionalized electrocatalysts enable stable acidic CO_2 electrolysis. *Nat. Catal.* **2023**, *6*, 763–772.

[124] Bai, J. P.; Cai, X. H.; Liu, X.; Singh, N.; Yao, L. B. Recent advances in microenvironment engineering for selective electrochemical C–N coupling. *ChemSusChem* **2025**, *18*, e202501366.

[125] Gerke, C. S.; Klenk, M.; Zapol, P.; Thoi, V. S. Pulsed-potential electrolysis enhances electrochemical C–N coupling by reorienting interfacial ions. *ACS Catal.* **2023**, *13*, 14540–14547.

[126] Bai, W. T.; Zeng, H. Y.; Chen, F. J.; Wu, S. S.; Wang, S. C.; Du, Y. P.; Liu, S. L.; Wang, D. S.; Dai, Z. H. Emerging atomistic modeling catalysts for C–N electrocatalysis. *Adv. Mater.* **2026**, *38*, e10907.

[127] Zhang, M. Y.; Zhu, W.; Liu, Z. Y.; Chen, S. R.; Zhou, D. Y.; Mu, X. Q.; Zhuang, Z. C.; Wang, S. C.; Yang, J. R.; Du, Y. P. et al. Selective sieving effect of multi-atomic bismuth interfaces for efficient formate electrosynthesis and evolution at industrial current density. *Angew. Chem., Int. Ed.* **2025**, *64*, e202510206.

[128] Liu, S. X.; Lu, J.; Yu, X.; Pang, H.; Zhang, Q.; Park, H. S. Rational design of metal-organic framework-nanoparticle composite electrocatalysts for sustainable nitrogen electrochemistry. *eScience* **2025**, *5*, 100378.

[129] Yang, H. C.; Duan, P. F.; Zhuang, Z. C.; Luo, Y. W.; Shen, J.; Xiong, Y. L.; Liu, X. W.; Wang, D. S. Understanding the dynamic evolution of active sites among single atoms, clusters, and nanoparticles. *Adv. Mater.* **2025**, *37*, 2415265.

[130] Wang, Y.; Ma, F. Y.; Zhang, G. Q.; Zhang, J. W.; Zhao, H.; Dong, Y. M.; Wang, D. S. Precise synthesis of dual atom sites for electrocatalysis. *Nano Res.* **2024**, *17*, 9397–9427.

[131] Wang, S. W.; Wang, L. G.; Zhou, X. D.; Fang, J. J.; Deng, C.; Wang, D. S. Design principles of single-atom catalysts anchored over porous materials for green catalysis and conversion. *Nano Res.* **2025**, *18*, 94907137.

[132] Tang, M. H.; Shen, J.; Zhang, F. T.; Zhao, Y. F.; Gan, T.; Zeng, W.; Li, R. X.; Wang, D. S.; Han, B. X.; Liu, Z. M. Upcycling of polyamide wastes to tertiary amines using mo single atoms and Rh nanoparticles. *Angew. Chem., Int. Ed.* **2025**, *64*, e202416436.

[133] Shen, J.; Tang, M. H.; Shi, Z. H.; Guan, S. Y.; Shi, Y. J.; Zhuang, Z. C.; Li, R. Z.; Yang, J. R.; He, D. P.; Liu, B. Z. et al. Efficient generation of negative hydrogen with bimetallic-ternary-structured catalysts for nitrobenzene hydrogenation. *Angew. Chem., Int. Ed.* **2025**, *64*, e202423626.

[134] Mao, D.; Wang, C.; Li, W.; Zhou, L.; Liu, J.; Zheng, Z. J.; Zhao, Y.; Cao, A. M.; Wang, S. T.; Huang, J. X. et al. Hollow multishelled structure: Synthesis chemistry and application. *Chem. Res. Chin. Univ.* **2024**, *40*, 346–393.

[135] Hou, P.; Yang, N. L.; Wang, D. Multi-functional hollow structures for intelligent drug delivery. *Chem. Res. Chin. Univ.* **2024**, *40*, 394–412.

[136] Su, F. M.; Wan, J. W.; Wang, D. Hollow multi-shelled structure photoelectric materials: Multiple shells bring novel properties. *Chem. Res. Chin. Univ.* **2024**, *40*, 413–427.

[137] Wang, H. Y.; Wei, P.; Wang, J. Y.; Wang, D. Hollow multishelled structure reviving lithium metal anode for high-energy-density batteries. *Chem. Res. Chin. Univ.* **2024**, *40*, 428–436.

[138] Wang, H.; Gong, G. N.; Sun, G. H.; Qi, J.; Yu, R. B.; Wang, D. Regulating oxygen vacancy defects in heterogeneous NiO–$CeO_{2-\delta}$ hollow multi-shelled structure for boosting oxygen evolution reaction. *Chem. Res. Chin. Univ.* **2024**, *40*, 475–483.